Fermi Gases with Synthetic Spin-Orbit Coupling

ARTICLE · NOVEMBER 2014

DOI: 10.1142/9789814590174_0002 · Source: arXiv

4 AUTHORS, INCLUDING:

Jing Zhang
Wuhan University
212 PUBLICATIONS **2,874** CITATIONS
SEE PROFILE

Hui Hu
Swinburne University of Technology
145 PUBLICATIONS **2,581** CITATIONS
SEE PROFILE

Xia-Ji Liu
Swinburne University of Technology
125 PUBLICATIONS **2,391** CITATIONS
SEE PROFILE

Fermi Gases with Synthetic Spin-Orbit Coupling

Jing Zhang
State Key Laboratory of Quantum Optics and Quantum Optics Devices, Institute of Opto-Electronics, Shanxi University, Taiyuan 030006, P. R. China

Hui Hu and Xia-Ji Liu
Centre for Atom Optics and Ultrafast Spectroscopy, Swinburne University of Technology, Melbourne 3122, Australia

Han Pu
Department of Physics and Astronomy, and Rice Quantum Institute, Rice University, Houston, TX 77251, USA

(Dated: November 14, 2014)

We briefly review recent progress on ultracold atomic Fermi gases with different types of synthetic spin-orbit coupling, including the one-dimensional (1D) equal weight Rashba-Dresselhaus and two-dimensional (2D) Rasbha spin-orbit couplings. Theoretically, we show how the single-body, two-body and many-body properties of Fermi gases are dramatically changed by spin-orbit coupling. In particular, the interplay between spin-orbit coupling and interatomic interaction may lead to several long-sought exotic superfluid phases at low temperatures, such as anisotropic superfluid, topological superfluid and inhomogeneous superfluid. Experimentally, only the first type - equal weight combination of Rasbha and Dresselhaus spin-orbit couplings - has been realized very recently using a two-photon Raman process. We show how to characterize a normal spin-orbit coupled atomic Fermi gas in both non-interacting and strongly-interacting limits, using particularly momentum-resolved radio-frequency spectroscopy. The experimental demonstration of a strongly-interacting spin-orbit coupled Fermi gas opens a promising way to observe various exotic superfluid phases in the near future.

PACS numbers: 05.30.Fk, 03.75.Hh, 03.75.Ss, 67.85.-d

Contents

I. Introduction 2

II. Theory of spin-orbit coupled Fermi gas 3
A. Theoretical framework 3
1. Functional path-integral approach 3
2. Two-particle physics from the particle-particle vertex function 5
3. Many-body T-matrix theory 6
4. Bogoliubov-de Gennes equation for trapped Fermi systems 7
5. Momentum- or spatially-resolved radio-frequency spectrum 8
B. 1D equal-weight Rashba-Dresselhaus spin-orbit coupling 9
1. Single-particle spectrum 10
2. Two-body physics 12
3. Momentum-resolved radio-frequency spectrum of the superfluid phase 13
4. Fulde-Ferrell superfluidity 15
5. 1D topological superfluidity 17
C. 2D Rashba spin-orbit coupling 19
1. Single-particle spectrum 20
2. Two-body physics 20
3. Crossover to rashbon BEC and anisotropic superfluidity 22
4. 2D Topological superfluidity 24

III. Experiments 25
A. The noninteracting spin-orbit coupled Fermi gas 26
1. Rabi oscillation 26
2. Momentum distribution 28
3. Lifshitz transition 28

4. Momentum-resolved rf spectrum 28
B. The strongly interacting spin-orbit coupled Fermi gas 30
1. Integrated radio-frequency spectrum 30
2. Coherent formation of Feshbach molecules by spin-orbit coupling 32

IV. Conclusion 32

Acknowledgments 33

References 33

I. INTRODUCTION

Modern physical theories describe reality in terms of fields, many of which obey gauge symmetry. Gauge symmetry is the property of a field theory in which different configurations of the underlying fields — which are not themselves directly observable — result in identical observable quantities. Electromagnetism is an ideal example to illustrate this point. A system of stationary electric charges produces an electric field $\mathbf{E}$ (but no magnetic field). It is convenient to define a scalar potential V, a voltage, that is also determined by the charge distribution. The electric field at any position is given by the gradient of the scalar potential: $\mathbf{E}(\mathbf{r}) = \nabla V(\mathbf{r})$. In this system, a global symmtry is readily perceived: if the scalar potential everywhere is changed by the same amount, i.e., $V(\mathbf{r}) \to V(\mathbf{r}) + V_0$, the resulting electric field is unchanged. A more non-trivial example is given by a system of moving charges which produces both electric and magnetic field. In addition to the scalar potential, we now also introduce a vector potential $\mathbf{A}$, the curl of which gives the magnetic field: $\mathbf{B}(\mathbf{r}) = \nabla \times \mathbf{A}(\mathbf{r})$. This system obeys the local gauge sysmmetry: any local change in the scalar potential $[V(\mathbf{r}) \to V(\mathbf{r}) - \partial\Lambda/\partial t$ with $\Lambda(\mathbf{r}, t)$ being an arbitrary function of position and time] can be combined with a compensating change in the vector potential $[\mathbf{A}(\mathbf{r}) \to \mathbf{A}(\mathbf{r}) + \nabla\Lambda]$ in such a way that the electric and magnetic fields are invariant.

Maxwell's classical theory of electromagnetism is the first gauge theory with local symmetry. A related symmetry can be demonstrated in the quantum theory of electromagnetic interactions, which describes the interaction between charged particles. From first sight, Maxwell's theory should not directly describe the center-of-mass motion of neutral atoms. However, a beautiful series of experiments carried out at NIST [1–3] demonstrated that artificial gauge fields can be generated in cold atomic vapours using laser fields, such that neutral atoms can be used to simulate charged particles moving in electromagnetic fields [4]. How to engineer artificial gauge fields is reviewed by Spielman in an article published in the previous volume of this book series [5].

It would not be very interesting if all light-induced gauge fields could do is to make neutral atoms mimic the behavior of charged particles. Indeed, artificial gauge field can be made non-Abelian, i.e., the Cartesian components of the field do not commute with each other. By contrast, the familiar electromagnetic fields are Abelian since their Cartesian components are represented by c-numbers, thus commuting with each other. A special feature of non-Abelian gauge field is that it can induce spin-orbit coupling. The concept of spin-orbit coupling (SOC) is encountered, for example, in the study of atomic structure, where the coupling between the electron's orbital motion and its intrinsic spin gives rise to the fine structure of atomic spectrum. In the current context, SOC refers to the coupling between the internal pseudo-spin degrees of freedom and the external motional degrees of freedom of the atom. That such SOC can be induced by laser fields can be easily understood as follows: The laser light induces transitions between atomic internal states, and in the meantime imparts photon's linear momentum to the atom. Thus the internal and the external degrees of freedom are coupled via their interaction with the photon.

SOC in cold atoms was first realized in a system of ^{87}Rb condensate by the NIST group in 2011 [6]. Since then, several groups have achieved SOC in both bosonic [7–10] and fermionic quantum gases [11–15]. SOC not only dramatically changes the single-particle dispersion relation, but is also the key ingredient underlying many interesting many-body phenomena and new materials such as topological insulators [16] and quantum spin Hall effects [17]. Due to the exquisite controllability of atomic systems, one can naturally expect that SOC in cold atoms will give rise to novel quantum states of matter and may lead to a deeper understanding of related phenomena in other systems. For this reason, spin-orbit coupled quantum gases have received tremendous attention over the past few years, and they no doubt represent one of the most active frontiers of cold atom research.

In this chapter, we will review the physics of spin-orbit coupled Fermi gas, both theoretically and experimentally. Although we will mainly focus on the research from our own groups, results from others will also be mentioned.

II. THEORY OF SPIN-ORBIT COUPLED FERMI GAS

We consider a spin-1/2 Fermi gas with SOC subject to attractively interaction between unlike spins. One great advantage of the atomic system is its unprecedented controllability. The interatomic interaction can be precisely tuned using the Feshbach resonance technique [18], which has already led to the discovery of the BEC-BCS crossover from a Bose-Einstein condensate (BEC) to a Bardeen-Cooper-Schrieffer (BCS) superfluid [19]. Different forms of SOC, many of which do not exist in natural materials, can also be engineered. The interplay between interatomic interactions and different forms of SOC may give rise to a number of intriguing physical phenomena. Here let us make some general remarks concerning the distinct features that can be brought out by SOC in a Fermi gas:

- SOC alters the single-particle dispersion which may lead to degenerate single-particle ground state, and may render the topology of the Fermi surface non-trivial [20].
- In the presence of attractive s-wave interaction, two fermions may form pairs. In general such pairs contain both singlet and triplet components [21–26] and have anisotropic (i.e., direction-dependent) effective mass [22–24]. In the many-body setting, a spin-orbit coupled superfluid Fermi gas contains both singlet and triplet pairing correlation [20, 22, 24, 27] and therefore may be regarded as an anisotropic superfluid [22].
- SOC may greatly enhance the pairing instability and hence dramatically increases the superfluid transition temperature [22, 23, 28].
- SOC, together with effective Zeeman fields, may generate exotic pairing [29–37] and/or topologically non-trivial superfluid state [38–55]. At the boundaries of topologically trivial and non-trivial regimes, exotic quasi-particle states (e.g., Majorana mode) may be created.

In the remaining part of this section, we will discuss two particular types of SOC. The first is the equal-weight Rashba-Dresselhaus SOC [56] which is the only one that has been experimentally realized so far. The second is the Rashba SOC which is of particular interest as it occurs naturally in certain semiconductor materials. However, before we do that, in the next subsection we first summarize the theoretical framework and explain the basics of momentum- or spatially-resolved radio-frequency (rf) spectroscopy, which turns out to be a very useful experimental tool for characterizing spin-orbit coupled interacting Fermi gases. For those readers who are interested in the physical consequences of a detailed type of SOC, this technical part may be skipped in their first reading.

A. Theoretical framework

In current experimental setups of ultracold atomic Fermi gases, the interactions between atoms are often tuned to be as strong as possible, in order to have an experimentally accessible superfluid transition temperature. With such strong interactions, there is a significant portion of Cooper pairs formed by two fermionic atoms with unlike spin. Theoretically, therefore, it is very crucial to treat atoms and Cooper pairs on an equal footing. Without SOC, a minimum theoretical framework for this purpose is the many-body T-matrix theory or pair-fluctuation theory [57–62]. In this subsection, we introduce briefly the essential idea of the pair-fluctuation theory using the functional path-integral approach and generalize the theory to include SOC [24]. Under this theoretical framework, both two- and many-body physics can be discussed in a unified fashion [24]. We also discuss the mean-field Bogoliubov-de Gennes equation, which represents a powerful tool for the study of trapped, inhomogeneous Fermi superfluids at low temperatures [42, 45, 47, 48, 50, 51].

1. Functional path-integral approach

Consider, for example, a three-dimensional (3D) spin-1/2 Fermi gas with mass m. The second-quantized Hamiltonian reads,

$$\mathcal{H} = \int d\mathbf{r} \left[\psi^{\dagger} \left(\hat{\xi}_{\mathbf{k}} + V_{\mathrm{SO}} \right) \psi + U_0 \, \psi_{\uparrow}^{\dagger} (\mathbf{r}) \, \psi_{\downarrow}^{\dagger} (\mathbf{r}) \, \psi_{\downarrow} (\mathbf{r}) \, \psi_{\uparrow} (\mathbf{r}) \right], \tag{1}$$

where $\hat{\xi}_{\mathbf{k}} \equiv \hat{\mathbf{k}}^2/(2m) - \mu = -\nabla^2/(2m) - \mu$ with the chemical potential μ, $\psi(\mathbf{r}) = [\psi_{\uparrow}(\mathbf{r}), \psi_{\downarrow}(\mathbf{r})]^T$ describes collectively the fermionic annihilation operator $\psi_{\sigma}(\mathbf{r})$ for spin-σ atom, and $V_{\mathrm{SO}}(\hat{\mathbf{k}})$ represents the spin-orbit coupling whose explicit form we do not specify here. The momentum $\hat{k}_{\alpha} \equiv -i\partial_{\alpha}$ ($\alpha = x, y, z$) should be regarded as the operators in real

space. For notational simplicity, we take $\hbar = 1$ throughout this paper. The last term in Eq. (1) represents the two-body contact s-wave interaction between unlike spins. The use of the contact interatomic interaction leads to an ultraviolet divergence at large momentum or high energy. To overcome such a divergence, we express the interaction strength U_0 in terms of the s-wave scattering length a_s,

$$\frac{1}{U_0} = \frac{m}{4\pi a_s} - \frac{1}{V}\sum_{\mathbf{k}} \frac{m}{\mathbf{k}^2}, \tag{2}$$

where V is the volume of the system.

The partition function of the system can be written as [61]

$$\mathcal{Z} = \int \mathcal{D}[\psi(\mathbf{r},\tau), \bar{\psi}(\mathbf{r},\tau)] \exp\left\{-\mathcal{S}\left[\psi(\mathbf{r},\tau), \bar{\psi}(\mathbf{r},\tau)\right]\right\}, \tag{3}$$

where the action

$$\mathcal{S}\left[\psi, \bar{\psi}\right] = \int_0^\beta d\tau \left[\int d\mathbf{r} \sum_\sigma \bar{\psi}_\sigma(\mathbf{r},\tau)\, \partial_\tau \psi_\sigma(\mathbf{r},\tau) + \mathcal{H}\left(\psi, \bar{\psi}\right)\right]. \tag{4}$$

is written as an integral over imaginary time τ. Here $\beta = 1/(k_B T)$ is the inverse temperature and $\mathcal{H}\left(\psi, \bar{\psi}\right)$ is obtained by replacing the field operators $\psi^\dagger$ and ψ with the Grassmann variables $\bar{\psi}$ and ψ, respectively. We can use the Hubbard-Stratonovich transformation to transform the quartic interaction term into a quadratic form as:

$$e^{-U_0 \int d\mathbf{r} d\tau \bar{\psi}_\uparrow \bar{\psi}_\downarrow \psi_\downarrow \psi_\uparrow} = \int \mathcal{D}\left[\Delta, \bar{\Delta}\right] \exp\left\{\int_0^\beta d\tau \int d\mathbf{r} \left[\frac{|\Delta(\mathbf{r},\tau)|^2}{U_0} + \left(\bar{\Delta}\psi_\downarrow\psi_\uparrow + \Delta\bar{\psi}_\uparrow\bar{\psi}_\downarrow\right)\right]\right\}, \tag{5}$$

from which the pairing field $\Delta(\mathbf{r},\tau)$ is defined.

Let us now introduce the 4-dimensional Nambu spinor $\Phi(\mathbf{r},\tau) \equiv [\psi_\uparrow, \psi_\downarrow, \bar{\psi}_\uparrow, \bar{\psi}_\downarrow]^T$ and rewrite the action as,

$$\mathcal{Z} = \int \mathcal{D}[\Phi, \bar{\Phi}; \Delta, \bar{\Delta}] \exp\left\{\int d\mathbf{r}' \int d\mathbf{r} \int_0^\beta d\tau' \int_0^\beta d\tau \left[\frac{1}{2}\bar{\Phi}(\mathbf{r},\tau) G^{-1} \Phi(\mathbf{r}',\tau') + \frac{|\Delta|^2}{U_0}\delta(\mathbf{r}-\mathbf{r}')\delta(\tau-\tau')\right] - \beta \sum_{\mathbf{k}} \hat{\xi}_{\mathbf{k}}\right\}, \tag{6}$$

where the 4×4 single-particle Green function is given by,

$$G^{-1} = \begin{bmatrix} -\partial_\tau - \hat{\xi}_{\mathbf{k}} - V_{\mathrm{SO}}(\hat{\mathbf{k}}) & i\Delta\hat{\sigma}_y \\ -i\bar{\Delta}\hat{\sigma}_y & -\partial_\tau + \hat{\xi}_{\mathbf{k}} + V_{\mathrm{SO}}^T(-\hat{\mathbf{k}}) \end{bmatrix} \delta(\mathbf{r}-\mathbf{r}')\delta(\tau-\tau'), \tag{7}$$

with the Pauli matrices $\hat{\sigma}_i$ $(i = 0, x, y, z)$ describing the spin degrees of freedom. The Nambu spinor representation treats equally the particle and the hole excitations. As a result, a zero-point energy appears in the last term of the action. Integrating out the original fermionic fields, we may rewrite the partition function as

$$\mathcal{Z} = \int \mathcal{D}[\Delta, \bar{\Delta}] \exp\left\{-\mathcal{S}_{\mathrm{eff}}\left[\Delta, \bar{\Delta}\right]\right\}, \tag{8}$$

where the effective action is given by

$$\mathcal{S}_{\mathrm{eff}}\left[\Delta, \bar{\Delta}\right] = \int_0^\beta d\tau \int d\mathbf{r} \left[-\frac{|\delta\Delta(\mathbf{r},\tau)|^2}{U_0}\right] - \frac{1}{2}\mathrm{Tr}\ln\left[-G^{-1}\right] + \beta\sum_{\mathbf{k}} \hat{\xi}_{\mathbf{k}}. \tag{9}$$

where the trace is taken over all the spin, spatial, and temporal degrees of freedom.

To proceed, we restrict ourselves to the Gaussian fluctuation and expand $\Delta(\mathbf{r},\tau) = \Delta_0(\mathbf{r}) + \delta\Delta(\mathbf{r},\tau)$. The effective action is then decomposed accordingly as $\mathcal{S}_{\mathrm{eff}} = \mathcal{S}_0 + \delta\mathcal{S}$, where the saddle-point action is

$$\mathcal{S}_0 = -\int_0^\beta d\tau \int d\mathbf{r} \frac{|\Delta_0(\mathbf{r})|^2}{U_0} - \frac{1}{2}\mathrm{Tr}\ln\left[-G_0^{-1}\right] + \beta\sum_{\mathbf{k}} \hat{\xi}_{\mathbf{k}} \tag{10}$$

and the pair-fluctuating action takes the form

$$\delta\mathcal{S} = \int_0^\beta d\tau \int d\mathbf{r} \left[-\frac{|\delta\Delta(\mathbf{r},\tau)|^2}{U_0} + \frac{1}{2}\left(\frac{1}{2}\right)\mathrm{Tr}\left(G_0\Sigma\right)^2\right] \tag{11}$$

with

$$\Sigma = \begin{pmatrix} 0 & i\delta\Delta\hat{\sigma}_y \\ -i\delta\bar{\Delta}\hat{\sigma}_y & 0 \end{pmatrix}. \tag{12}$$

Here G_0^{-1} is the inverse mean-field Green function and has the same form as G^{-1} in Eq. (7) with $\Delta(\mathbf{r},\tau)$ replaced by $\Delta_0(\mathbf{r})$. We note that the static pairing field $\Delta_0(\mathbf{r})$ can be either homogeneous or inhomogeneous. In the latter case, a typical form is $\Delta_0(\mathbf{r}) = \Delta_0 e^{i\mathbf{q}\cdot\mathbf{r}}$, referred to as the Fulde-Ferrell superfluid [63], in which the Cooper pairs condense into a state with nonzero center-of-mass momentum $\mathbf{q}$.

Let us now focus on a homogeneous system, where the momentum is a good quantum number so that we take $\xi_{\mathbf{k}} = \hat{\xi_{\mathbf{k}}}$ and $V_{\mathrm{SO}}(\mathbf{k}) = V_{\mathrm{SO}}(\hat{\mathbf{k}})$. The fluctuating part of the effective action may be formally written in terms of the many-body particle-particle vertex function $\Gamma(\mathbf{q}, i\nu_n)$ [61],

$$\delta\mathcal{S} = k_B T \sum_{Q=(\mathbf{q},i\nu_n)} \left[-\Gamma^{-1}(Q)\right] \delta\Delta(Q)\delta\bar{\Delta}(Q), \tag{13}$$

where $Q \equiv (\mathbf{q}, i\nu_n)$ and ν_n is the bosonic Matsubara frequency. By integrating out the quadratic term in δS, we obtain the contribution from the Gaussian pair fluctuations to the thermodynamic potential as [61]

$$\delta\Omega = k_B T \sum_{\mathbf{q},i\nu_n} \ln\left[-\Gamma^{-1}(\mathbf{q}, i\nu_n)\right]. \tag{14}$$

Within the Gaussian pair fluctuation approximation, naïvely, the vertex function may be interpreted as the Green function of "Cooper pairs". This idea is supported by Eq. (14), as the thermodynamic potential Ω_B of a free bosonic Green function $\mathcal{G}_B$ is formally given by $\Omega_B = k_B T \sum_{\mathbf{q},i\nu_n} \ln[-\mathcal{G}_B^{-1}(\mathbf{q}, i\nu_n)]$. At this point, the advantage of using pair-fluctuation theory becomes evident. For the fermionic degree of freedom, we simply work out the single-particle Green function G_0 and the related mean-field thermodynamic potential $\Omega_0 = k_B T \mathcal{S}_0$. An example will be provided later on in the study of the Fulde-Ferrell superfluidity. While for Cooper pairs, we calculate the vertex function and the fluctuating thermodynamic potential $\delta\Omega$. In this way, we may obtain a satisfactory description of strongly-interacting Fermi systems [59, 60, 62].

In the normal state where the pairing field vanishes, i.e., $\Delta_0 = 0$, we may obtain the explicit expression of the vertex function. In this case, the inverse Green function G_0^{-1} has a diagonal form and can be easily inverted to give [24]:

$$G_0(K) = \begin{pmatrix} \left[i\omega_m - \xi_{\mathbf{k}} - V_{\mathrm{SO}}(\mathbf{k})\right]^{-1} & 0 \\ 0 & \left[i\omega_m + \xi_{\mathbf{k}} + V_{\mathrm{SO}}^T(-\mathbf{k})\right]^{-1} \end{pmatrix} \equiv \begin{bmatrix} \mathcal{G}_0(K) & 0 \\ 0 & \tilde{\mathcal{G}}_0(K) \end{bmatrix}, \tag{15}$$

where $K \equiv (\mathbf{k}, i\omega_m)$ and ω_m is the fermionic Matsubara frequency. Here we have introduced the 2×2 particle Green function $\mathcal{G}_0(K)$ and hole Green function $\tilde{\mathcal{G}}_0(K)$, which are related to each other by $\tilde{\mathcal{G}}_0(K) = -[\mathcal{G}_0(-K)]^T$. It is straightforward to show that,

$$\Gamma^{-1}(Q) = \frac{1}{U_0} + \frac{k_B T}{2} \sum_{K=(\mathbf{k},i\omega_m)} \left[\mathcal{G}_0(K)(i\hat{\sigma}_y)\tilde{\mathcal{G}}_0(K-Q)(i\hat{\sigma}_y)\right]. \tag{16}$$

The detailed expression of the vertex function depends on the type of SOC. In the study of Rashba SOC, we will give an example that shows how to calculate the vertex function.

2. Two-particle physics from the particle-particle vertex function

The vertex function can describe the pairing instability of Cooper pairs both on the Fermi surface and in the vacuum. In the latter case, it describes exactly the two-particle state. The corresponding two-body inverse vertex function $\Gamma_{\mathrm{2b}}^{-1}(Q)$ can be obtained from the many-body inverse vertex function by discarding the Fermi distribution function and by setting chemical potential $\mu = 0$ [64]. One important question concerning the two-body state is whether there exist bound states. For a given momentum $\mathbf{q}$, the bound state energy $E(\mathbf{q})$ can be determined from the two-particle vertex function using the following relation ($i\nu_n \to \omega + i0^+$) [22, 24]:

$$\mathrm{Re}\left\{\Gamma_{\mathrm{2b}}^{-1}[\mathbf{q}; \omega = E(\mathbf{q})]\right\} = 0. \tag{17}$$

A true bound state must satisfy $E(\mathbf{q}) < 2E_{\min}$ where $E_{\min}$ is the single-particle ground state energy.

It is straightforward but lengthy to calculate the two-particle vertex function for any type of SOC. Here, we quote only the energy equation obtained using Eq. (17) for the most general form of SOC [34],

$$V_{\mathrm{SO}}\left(\hat{\mathbf{k}}\right) = \sum_{i=x,y,z} \left(\lambda_i \hat{k}_i + h_i\right) \hat{\sigma}_i \,, \tag{18}$$

where λ_i is the strength of SOC in the direction $i = (x, y, z)$ and h_i denotes the effective Zeeman field. The eigenenergy $E(\mathbf{q})$ of a two-body eigenstate with momentum $\mathbf{q}$ satisfies the equation:

$$\frac{m}{4\pi a_s} = \frac{1}{V}\sum_{\mathbf{k}} \left[\left(\mathcal{E}_{\mathbf{k},\mathbf{q}} - \frac{4\mathcal{E}_{\mathbf{k},\mathbf{q}}^2 (\boldsymbol{\lambda}\cdot\mathbf{k})^2 - 4\left[\sum_{i=x,y,z} \lambda_i k_i (\lambda_i q_i + 2h_i)\right]^2}{\mathcal{E}_{\mathbf{k},\mathbf{q}}\left[\mathcal{E}_{\mathbf{k},\mathbf{q}}^2 - \sum_{i=x,y,z}(\lambda_i q_i + 2h_i)^2\right]} \right)^{-1} + \frac{1}{2\epsilon_{\mathbf{k}}} \right] , \tag{19}$$

where $\mathcal{E}_{\mathbf{k},\mathbf{q}} \equiv E(\mathbf{q}) - \epsilon_{\frac{\mathbf{q}}{2}+\mathbf{k}} - \epsilon_{\frac{\mathbf{q}}{2}-\mathbf{k}}$ and $\epsilon_{\mathbf{k}} = k^2/(2m)$. We note that, in general, the lowest-energy two-particle state may occur at a finite momentum $\mathbf{q}$. That is, the two-particle bound state could have a nonzero center-of-mass momentum. Later, we shall see that this unusual property has nontrivial consequences in the many-body setting. Another peculiar feature of the two-particle bound state is that the pairs may have an effective mass larger than $2m$. For example, for the bound state with zero center-of-mass momentum $\mathbf{q} = 0$, it would have a quadratic dispersion for small $\mathbf{p}$,

$$E(\mathbf{p}) = E(\mathbf{0}) + \frac{p_x^2}{2M_x} + \frac{p_y^2}{2M_y} + \frac{p_z^2}{2M_z}. \tag{20}$$

The effective mass of the bound state M_i $(i = x, y, z)$ can then be determined directly from this dispersion relation.

Another approach to study the two-particle state with SOC , more familiar to most readers, is to use the following ansatz for the two-particle wave function [21, 23, 65, 66],

$$|\Phi_{2B}\rangle = \frac{1}{\sqrt{\mathcal{C}}}\sum_{\mathbf{k}} \left[\psi_{\uparrow\downarrow}(\mathbf{k})\, c^\dagger_{\frac{\mathbf{q}}{2}+\mathbf{k}\uparrow} c^\dagger_{\frac{\mathbf{q}}{2}-\mathbf{k}\downarrow} + \psi_{\downarrow\uparrow}(\mathbf{k})\, c^\dagger_{\frac{\mathbf{q}}{2}+\mathbf{k}\downarrow} c^\dagger_{\frac{\mathbf{q}}{2}-\mathbf{k}\uparrow} + \psi_{\uparrow\uparrow}(\mathbf{k})\, c^\dagger_{\frac{\mathbf{q}}{2}+\mathbf{k}\uparrow} c^\dagger_{\frac{\mathbf{q}}{2}-\mathbf{k}\uparrow} + \psi_{\downarrow\downarrow}(\mathbf{k})\, c^\dagger_{\frac{\mathbf{q}}{2}+\mathbf{k}\downarrow} c^\dagger_{\frac{\mathbf{q}}{2}-\mathbf{k}\downarrow}\right] |\mathrm{vac}\rangle \,, \tag{21}$$

where $c^\dagger_{\mathbf{k}\uparrow}$ and $c^\dagger_{\mathbf{k}\downarrow}$ are creation field operators of spin-up and spin-down atoms with momentum $\mathbf{k}$ and $\mathcal{C}$ is the normalization factor. We note that, in the presence of SOC, the wave function of the two-particle state has both spin singlet and triplet components. Then, using the Schrödinger equation $\mathcal{H}\,|\Phi_{2B}(\mathbf{q})\rangle = E(\mathbf{q})\,|\Phi_{2B}(\mathbf{q})\rangle$, we can straightforwardly derive the equations for coefficients $\psi_{\sigma\sigma'}$ appearing in the above two-body wave function and then the energy equation for $E(\mathbf{q})$. For the general form of SOC, Eq. (18), it leads to exactly the same energy equation (19) [34].

Each of the two approaches mentioned above has its own advantages. The vertex function approach is useful to understand the relationship between the two-body physics and the many-body physics. For example, it can be used to obtain the two-particle bound state in the presence of a Fermi surface. The latter approach of using the two-particle Schrödinger equation naturally yields the two-particle wave function. Both approaches have been used extensively in the literature.

3. Many-body T-matrix theory

The functional path-integral approach gives the simplest version of the many-body T-matrix theory, where the *bare* Green function has been used in the vertex function. Here, for completeness, we mention briefly another partially self-consistent T-matrix scheme for a normal spin-orbit coupled Fermi gas, by taking one bare and one fully dressed Green function in the vertex function [13, 28]. In this scheme, we have the Dyson equation,

$$\mathcal{G}(K) = \left[\mathcal{G}_0^{-1}(K) - \Sigma(K)\right]^{-1}, \tag{22}$$

where the self-energy is given by

$$\Sigma(K) = k_B T \sum_{Q=(\mathbf{q},i\nu_n)} t(Q)(i\hat{\sigma}_y)\tilde{\mathcal{G}}_0(K-Q)(i\hat{\sigma}_y) \tag{23}$$

and $\tilde{\mathcal{G}}_0(K) \equiv -[\mathcal{G}_0(-K)]^T$. Here $t(Q) \equiv U_0/[1 + U_0\chi(Q)]$ is the (scalar) T-matrix with a two-particle propagator

$$\chi(Q) = \frac{k_B T}{2} \sum_{K=(\mathbf{k}, i\omega_m)} \mathrm{Tr}\left[\mathcal{G}(K)\,(i\hat{\sigma}_y)\,\tilde{\mathcal{G}}_0(K-Q)\,(i\hat{\sigma}_y)\right], \tag{24}$$

where the trace is taken over the spin degree of freedom only. Note that a fully self-consistent T-matrix theory may also be obtained by replacing in Eqs. (23) and (24) the bare Green function $\tilde{\mathcal{G}}_0(K-Q)$ with the fully dressed Green function $\tilde{\mathcal{G}}(K-Q)$. We note also that Eqs. (22)-(24) provide a natural generalization of the well-known many-body T-matrix theory [62], by including the effect of SOC, where the particle or hole Green function, $\mathcal{G}(K)$ or $\tilde{\mathcal{G}}(K)$, now becomes a 2×2 matrix.

In general, the partially self-consistent T-matrix equations are difficult to solve [62]. At a *qualitative* level, we may adopt a pseudogap decomposition advanced by the Chicago group [67] and approximate the T-matrix $t(Q) = t_{sc}(Q) + t_{pg}(Q)$ to be the sum of two parts. Here $t_{sc}(Q) = -(\Delta_{sc}^2/T)\delta(Q)$ is the contribution from the superfluid with Δ_{sc} being the superfluid order parameter, and $t_{pg}(Q)$ represents the contribution from un-condensed pairs which give rise to a pseudogap

$$\Delta_{pg}^2 \equiv -k_B T \sum_{Q \neq 0} t_{pg}(Q)\,. \tag{25}$$

The full pairing order parameter is given by $\Delta_0^2 = \Delta_{sc}^2 + \Delta_{pg}^2$. Accordingly, we have the self-energy $\Sigma(K) = \Sigma_{sc}(K) + \Sigma_{pg}(K)$, where

$$\Sigma_{sc} = -\Delta_{sc}^2 (i\sigma_y)\tilde{\mathcal{G}}_0(K)(i\sigma_y) \tag{26}$$

and

$$\Sigma_{pg} = -\Delta_{pg}^2 (i\sigma_y)\tilde{\mathcal{G}}_0(K)(i\sigma_y). \tag{27}$$

We note that, at zero temperature the pseudogap approximation is simply the standard mean-field BCS theory, in which $\Sigma(K) = -\Delta_0^2(i\sigma_y)\tilde{\mathcal{G}}_0(K)(i\sigma_y)$. Above the superfluid transition, however, it captures the essential physics of fermionic pairing and therefore should be regarded as an improved theory beyond mean-field. To calculate the pseudogap Δ_{pg}, we approximate

$$t_{pg}^{-1}(Q \simeq 0) = \mathcal{Z}\left[i\nu_n - \Omega_{\mathbf{q}} + \mu_{pair}\right],$$

where the residue $\mathcal{Z}$ and the effective dispersion of pairs $\Omega_{\mathbf{q}} = q^2/2M^*$ are to be determined by expanding $\chi(Q)$ about $Q = 0$ in the case that the Cooper pairs condense into a zero-momentum state. The form of $t_{pg}(Q)$ leads to

$$\Delta_{pg}^2(T) = \mathcal{Z}^{-1} \sum_{\mathbf{q}} f_B(\Omega_{\mathbf{q}} - \mu_{pair}),$$

where $f_B(x) \equiv 1/(e^{x/k_B T} - 1)$ is the bosonic distribution function. We finally obtain two coupled equations, the gap equation $1/U_0 + \chi(Q=0) = \mathcal{Z}\mu_{pair}$ and the number equation $n = k_B T \sum_K \mathrm{Tr}\mathcal{G}(K)$, from which the superfluid order parameter Δ_{sc} and the chemical potential μ can be determined. This pseudogap method has been used to study the thermodynamics and momentum-resolved rf spectroscopy of interacting Fermi gases with different types of SOC [13, 28].

4. Bogoliubov-de Gennes equation for trapped Fermi systems

All cold atom experiments are performed with some trapping potentials, $V_T(\mathbf{r})$. For such inhomogeneous systems, it is difficult to directly consider pair fluctuations. In most cases, we focus on the mean-field theory by using the saddle-point thermodynamic potential Eq. (10) and minimizing it to determine the order parameter $\Delta_0(\mathbf{r})$. This amounts to diagonalizing the 4×4 single-particle Green function $G_0^{-1}(\mathbf{r}, \tau; \mathbf{r}', \tau')$ with the standard Bogoliubov transformation,

$$\alpha_\eta = \int d\mathbf{r} \sum_\sigma \left[u_{\sigma\eta}(\mathbf{r})\,\psi_\sigma(\mathbf{r}) + \nu_{\sigma\eta}(\mathbf{r})\,\psi_\sigma^\dagger(\mathbf{r})\right], \tag{28}$$

where α_η is the field operator for Bogoliubov quasiparticle with energy E_η and Nambu spinor wave function $\Phi_\eta(\mathbf{r}) \equiv [u_{\uparrow\eta}(\mathbf{r}), u_{\downarrow\eta}(\mathbf{r}), v_{\uparrow\eta}(\mathbf{r}), v_{\downarrow\eta}(\mathbf{r})]^T$, which satisfies the following Bogoliubov-de Gennes (BdG) equation,

$$\begin{bmatrix} -\nabla^2/(2m) - \mu + V_T(\mathbf{r}) + V_{\rm SO}(\hat{\mathbf{k}}) & -i\Delta_0(\mathbf{r})\hat{\sigma}_y \\ i\Delta_0^*(\mathbf{r})\hat{\sigma}_y & \nabla^2/(2m) + \mu - V_T(\mathbf{r}) - V_{\rm SO}^T(-\hat{\mathbf{k}}) \end{bmatrix} \Phi_\eta(\mathbf{r}) = E_\eta \Phi_\eta(\mathbf{r}). \tag{29}$$

The BdG Hamiltonian in the above equation includes the pairing gap function $\Delta_0(\mathbf{r})$ that should be determined self-consistently. For this purpose, we may take the inverse Bogoliubov transformation and obtain

$$\psi_\sigma(\mathbf{r}) = \sum_\eta \left[u_{\sigma\eta}(\mathbf{r})\alpha_\eta + \nu_{\sigma\eta}^*(\mathbf{r})\alpha_\eta^\dagger\right]. \tag{30}$$

The gap function $\Delta_0(\mathbf{r}) = -U_0\langle\psi_\downarrow(\mathbf{r})\psi_\uparrow(\mathbf{r})\rangle$ is then given by,

$$\Delta_0(\mathbf{r}) = -\frac{U_0}{2}\sum_\eta \left[u_{\uparrow\eta}(\mathbf{r})v_{\downarrow\eta}^*(\mathbf{r})f(E_\eta) + u_{\downarrow\eta}(\mathbf{r})v_{\uparrow\eta}^*(\mathbf{r})f(-E_\eta)\right], \tag{31}$$

where $f(E) \equiv 1/[e^{E/(k_BT)}+1]$ is the Fermi distribution function at temperature T. Accordingly, the total density takes the form,

$$n(\mathbf{r}) = \frac{1}{2}\sum_{\sigma\eta}\left[|u_{\sigma\eta}(\mathbf{r})|^2 f(E_\eta) + |v_{\sigma\eta}(\mathbf{r})|^2 f(-E_\eta)\right]. \tag{32}$$

The chemical potential μ can be determined using the number equation, $N = \int d\mathbf{r} n(\mathbf{r})$. This BdG approach has been used to investigate topological superfluids in harmonically trapped spin-orbit coupled Fermi gases in 1D and 2D [42, 45, 47, 48, 50, 51]. It will be discussed in greater detail in later sections.

It is important to note that, the use of Nambu spinor representation enlarges the Hilbert space of the system. As a result, there is an intrinsic particle-hole symmetry in the Bogoliubov solutions: For any "particle" solution with wave function $\Phi_\eta^{(p)}(\mathbf{r}) = [u_{\uparrow\eta}(\mathbf{r}), u_{\downarrow\eta}(\mathbf{r}), v_{\uparrow\eta}(\mathbf{r}), v_{\downarrow\eta}(\mathbf{r})]^T$ and energy $E_\eta^{(p)} \geq 0$, we can always find a partner "hole" solution with wave function $\Phi_\eta^{(h)}(\mathbf{r}) = [v_{\uparrow\eta}^*(\mathbf{r}), v_{\downarrow\eta}^*(\mathbf{r}), u_{\uparrow\eta}^*(\mathbf{r}), u_{\downarrow\eta}^*(\mathbf{r})]^T$ and energy $E_\eta^{(h)} = -E_\eta^{(p)} \leq 0$. These two solutions correspond exactly to the same physical state. To remove this redundancy, we have added an extra factor of $1/2$ in the expressions for pairing gap function Eq. (31) and total density Eq. (32). As we shall see, this particle-hole symmetry is essential to the understanding of the appearance of exotic Majorana fermions - particles that are their own antiparticles - in topological superfluids.

5. *Momentum- or spatially-resolved radio-frequency spectrum*

Radio-frequency (rf) spectroscopy, including both momentum-resolved and spatially-resolved rf-spectroscopy, is a powerful tool to characterize interacting many-body systems. It has been widely used to study fermionic pairing in a two-component atomic Fermi gas near Feshbach resonances in the BEC-BCS crossover [68–72]. Most recently, it has also been used to detect new quasiparticles known as repulsive polarons [73, 74], which occur when "impurity" fermionic particles interact repulsively with a fermionic environment.

The underlying mechanism of rf-spectroscopy is rather simple. The rf field drives transitions between one of the hyperfine states (say, $|\downarrow\rangle$) and an empty hyperfine state $|3\rangle$ which lies above it by an energy $\omega_{3\downarrow}$. The Hamiltonian describing this rf-coupling may be written as,

$$\mathcal{V}_{\rm rf} = V_0\int d\mathbf{r}\left[\psi_3^\dagger(\mathbf{r})\psi_\downarrow(\mathbf{r}) + \psi_\downarrow^\dagger(\mathbf{r})\psi_3(\mathbf{r})\right], \tag{33}$$

where V_0 is the strength of the rf drive. For a weak rf field, the number of transferred atoms may be calculated using linear response theory. At this point, it is important to note that a final state effect might be present, which is caused by the interaction between atoms in the final third state and those in the initial spin-up or spin-down state. This final state effect is significant for ^{6}Li atoms; while for ^{40}K atoms, it is not important [19].

For momentum-resolved rf spectroscopy [71], the momentum distribution of the transferred atoms can be obtained by absorption imaging after a time-of-flight. This gives rise to the information about the single-particle spectral function of spin-down atoms of the original Fermi system, $\mathcal{A}_{\downarrow\downarrow}(\mathbf{k},\omega)$. In the absence of the final-state effect, the rf transfer strength $\Gamma(\mathbf{k},\omega)$ at a given momentum is given by,

$$\Gamma(\mathbf{k},\omega) = \mathcal{A}_{\downarrow\downarrow}(\mathbf{k}, \epsilon_{\mathbf{k}} - \mu - \omega + \omega_{3\downarrow}) f(\epsilon_{\mathbf{k}} - \mu - \omega + \omega_{3\downarrow}). \tag{34}$$

Here, we have assumed that the atoms in the third state have the dispersion relation $\epsilon_{\mathbf{k}} = k^2/(2m)$ in free space and have taken the coupling strength $V_0 = 1$. Experimentally, we can either measure the momentum-resolved rf spectroscopy along a particular direction, say, the x-direction, by integrating along the two perpendicular directions

$$\Gamma(k_x, \omega) \equiv \sum_{k_y, k_z} \Gamma(\mathbf{k}, \omega), \tag{35}$$

or after integrating along the remaining direction, obtain the fully integrated rf spectrum $\Gamma(\omega) \equiv \sum_{\mathbf{k}} \Gamma(\mathbf{k}, \omega)$. We note that, in the extremely weakly interacting BCS and BEC regimes, where the physics is dominated by single-particle or two-particle physics, respectively, we may use the Fermi golden rule to calculate the momentum-resolved rf spectroscopy. This will be discussed in greater detail in the relevant subsections. We note also that momentum-resolved rf spectroscopy is precisely an ultracold atomic analogue of the well-known angle-resolved photoemission spectroscopy (ARPES) widely used in solid-state experiments.

Alternatively, we may use rf spectroscopy to probe the local information about the original Fermi system. This was first demonstrated in measuring the pairing gap by using phase-contrast imaging within the local density approximation for a trapped Fermi gas [69]. A more general idea is to use a specifically designed third state, which has a very flat dispersion relation [75]. This leads to a spatially-resolved rf spectroscopy, which measures precisely the local density of states of the Fermi system,

$$\rho_\sigma(\mathbf{r}, \omega) = \frac{1}{2} \sum_\eta \left[|u_{\sigma\eta}(\mathbf{r})|^2 \delta(\omega - E_\eta) + |v_{\sigma\eta}(\mathbf{r})|^2 \delta(\omega + E_\eta) \right]. \tag{36}$$

It could be regarded as a cold-atom scanning tunneling microscopy (STM). As we shall see, the spatially-resolved rf spectroscopy will provide a useful although indirect measurement of the long-sought Majorana fermion in atomic topological superfluids.

B. 1D equal-weight Rashba-Dresselhaus spin-orbit coupling

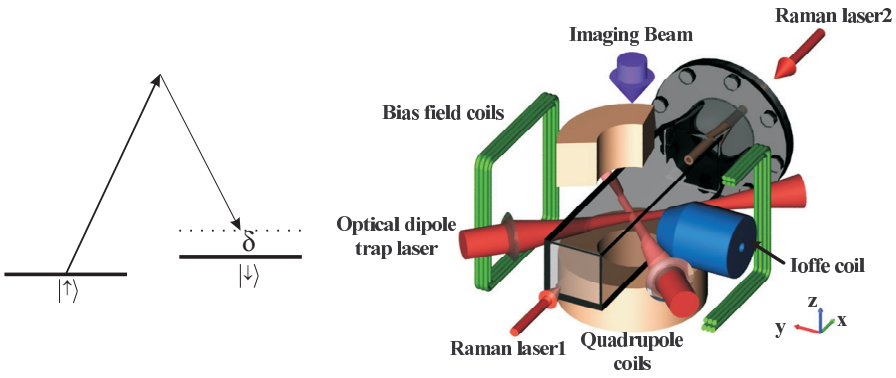

FIG. 1: Left panel: schematic of the Raman transition that produced the equal-weight Rashba-Dresselhaus SOC. The two atomic states are labeled as $|\uparrow\rangle$ and $|\downarrow\rangle$. δ is the two-photon Raman detuning. Right panel: schematic of the experimental setup where a pair of Raman beams counter-propagate along the x-axis. Right figure taken from Ref. [11].

Let us now discuss the two specific types of SOC. One simple scheme to create SOC in cold atoms is through a Raman transition that couples two hyperfine ground states of the atom, as schematically shown in Fig. 1. The Raman process is described by the following single-particle Hamiltonian in the first-quantization representation

$$\mathcal{H}_0 = \frac{\hat{\mathbf{p}}^2}{2m} + \frac{1}{2} \begin{pmatrix} \delta & \Omega e^{i2k_r x} \\ \Omega e^{-i2k_r x} & -\delta \end{pmatrix}, \tag{37}$$

where $\hat{\mathbf{p}}$ is the momentum operator of the atom, $2k_r\hat{x}$ is the photon recoil momentum taken to be along the x-axis, δ and Ω are the two-photon detuning and the coupling strength of the Raman beams, respectively. The Hamiltonian acts on the Hilbert space expanded by the spin-up and spin-down basis, $|\uparrow\rangle$ and $|\downarrow\rangle$. By applying a unitary transformation with

$$U = \begin{pmatrix} e^{ik_r x} & 0 \\ 0 & e^{-ik_r x} \end{pmatrix}, \tag{38}$$

the Hamiltonian $\mathcal{H}_0$ can be recast into the following form:

$$\mathcal{H}_{\rm SO} = U^\dagger \mathcal{H}_0 U = \frac{\left(\hat{k}_x + k_r\hat{\sigma}_z\right)^2}{2m} + \frac{\left(\hat{k}_y^2 + \hat{k}_z^2\right)}{2m} + \frac{\Omega}{2}\hat{\sigma}_x + \frac{\delta}{2}\hat{\sigma}_z\,. \tag{39}$$

Here, $\hat{\mathbf{k}} = (\hat{k}_x, \hat{k}_y, \hat{k}_z)$ denotes the quasi-momentum operator of the atom: When $\hat{\mathbf{k}}$ is applied to the transformed wave function, it gives the atomic quasi-momentum $\mathbf{k}$ that is related to the real momentum $\mathbf{p}$ as $\hat{\mathbf{p}} = (\hat{\mathbf{k}} \pm k_r\hat{x})$ with $\pm$ for spin-up and down, respectively. From this expression, it is sometimes convenient to regard both Ω and δ as the strengths of effective Zeeman fields.

We note that after a pseudo-spin rotation ($\sigma_z \to \sigma_x$, $\sigma_x \to -\sigma_z$), Hamiltonian (39) can be cast into the general form of SOC in Eq. (18) with $\boldsymbol{\lambda} = (k_r^2/m, 0, 0)$ and $\boldsymbol{h} = (\delta/2, 0, -\Omega/2)$. It is clear that the SOC is along a specific direction. Actually, it is an equal-weight combination of the well-known Rashba and Dresselhaus SOCs in solid-state physics [56]. For this reason, hereafter we would refer to it as 1D equal-weight Rashba-Dresselhaus SOC. We may also refer to the detuning δ as the in-plane Zeeman field since it is aligned along the same direction as the SOC. Accordingly, we call the coupling strength Ω as the out-of-plane Zeeman field. As we shall see, depending on δ and Ω, the spin-orbit coupled Fermi system can display distinct quantum superfluid phases at low temperatures.

1. *Single-particle spectrum*

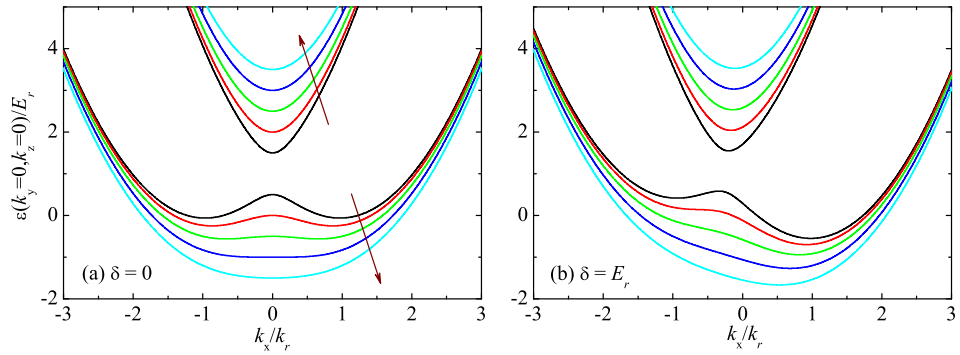

FIG. 2: Single particle spectrum of a Fermi gas with 1D equal-weight Rashba-Dresselhaus SOC, with (a) or without detuning (b). In each panel, we increase the coupling strength of the Raman beams from E_r to $5E_r$, with a step of E_r, as indicated by the arrows.

The single-particle spectrum can be easily obtained by diagonalizing the Hamiltonian (39), which is given by

$$E_{\mathbf{k}\pm} = E_r + \frac{\mathbf{k}^2}{2m} \pm \sqrt{\left(\frac{\Omega}{2}\right)^2 + \left(\lambda k_x + \frac{\delta}{2}\right)^2}\,, \tag{40}$$

where we have defined a recoil energy $E_r \equiv k_r^2/(2m)$ and an SOC strength $\lambda \equiv k_r/m$. The spectrum contains two branches as shown in Fig. 2. For small Ω, the lower branch exhibits a double-well structure. The double wells are symmetric (asymmetric) for $\delta = 0$ ($\delta \neq 0$). For large Ω, the two wells in the lower branch merge into a single one. It is important to emphasize that in each branch atoms stay at a mixed spin state with both spin-up and down components.

The single-particle spectrum can be easily measured by using momentum-resolved rf spectroscopy, as already shown at Shanxi University and MIT [11, 12]. In this case, the number of transferred atoms can be calculated by using the Fermi's golden rule [76]:

$$\Gamma\left(k_x, \omega\right) = \sum_{i,f} \left|\langle\Phi_f|\,\mathcal{V}_{rf}\,|\Phi_i\rangle\right|^2 f\left(E_i - \mu\right)\delta\left[\omega - \omega_{3\downarrow} - \left(E_f - E_i\right)\right], \tag{41}$$

where the summation is over all possible initial single-particle states Φ_i (with energy E_i and a given wavevector k_x) and final states Φ_f (with energy E_f), and the Dirac δ-function ensures energy conservation during the rf transition. In practice, the δ-function is replaced by a function with finite width (e.g., $\delta(x) \to (\gamma/\pi)(x^2+\gamma^2)^{-1}$ where γ accounts for

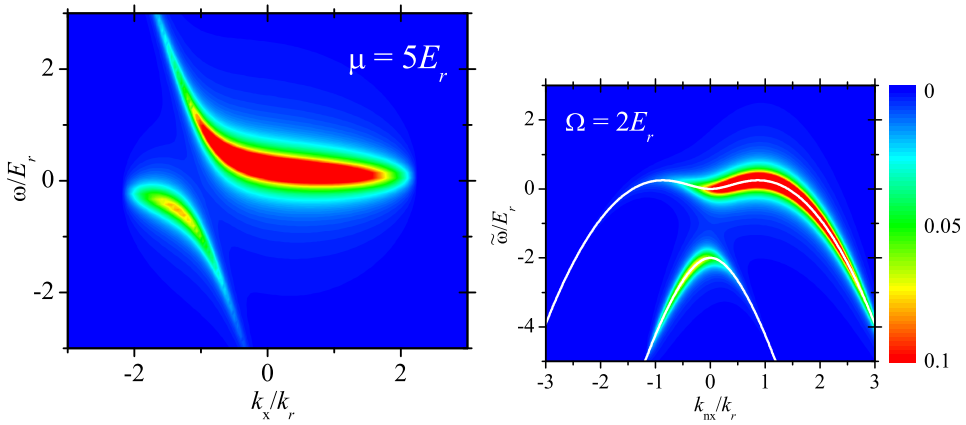

FIG. 3: Theoretical simulation on momentum-resolved rf spectroscopy of a Fermi gas with 1D equal-weight Rashba-Dresselhaus SOC. Left panel: simulated experimental spectroscopy $\Gamma(k_x, \omega)$. Right panel: the spectroscopy $\Gamma(k_{nx} \equiv k_x + k_r, \tilde{\omega} = \omega + k_x^2/2m)$. Here, the intensity of the contour plot shows the number of transferred atoms, increasingly linearly from 0 (blue) to its maximum value (red). We have set $\omega_{3\downarrow} = 0$ and used a Lorentzian distribution to replace the Delta function. Figure taken from Ref. [76] with modification.

the energy resolution of the measurement). The single-particle wave function Φ_i is known from the diagonalization of the Hamiltonian (39) and the transfer element $\langle \Phi_f | \mathcal{V}_{rf} | \Phi_i \rangle$ is then easy to determine. The left panel of Fig. 3 shows the predicted momentum-resolved spectroscopy $\Gamma(k_x, \omega)$ at $\delta = 0$ and $\Omega = 2E_r$. The chemical potential is tuned ($\mu = 5E_r$) in such a way that there are significant populations in both energy branches. The simulated spectrum is not straightforward to understand, because of the final free-particle dispersion relation in the energy conservation in Eq. (41) and also the recoil momentum shift (k_r) arising from the unitary transformation Eq. (38). Therefore, it is useful to define

$$\tilde{\Gamma}(k_{nx}, \tilde{\omega}) \equiv \Gamma\left(k_x + k_r, \omega + \frac{k_x^2}{2M}\right), \tag{42}$$

for which, the energy conservation takes the form $\delta[\tilde{\omega} + E_i(k_x)]$. As shown on the right panel of Fig. 3, the single-particle spectrum is now clearly visible.

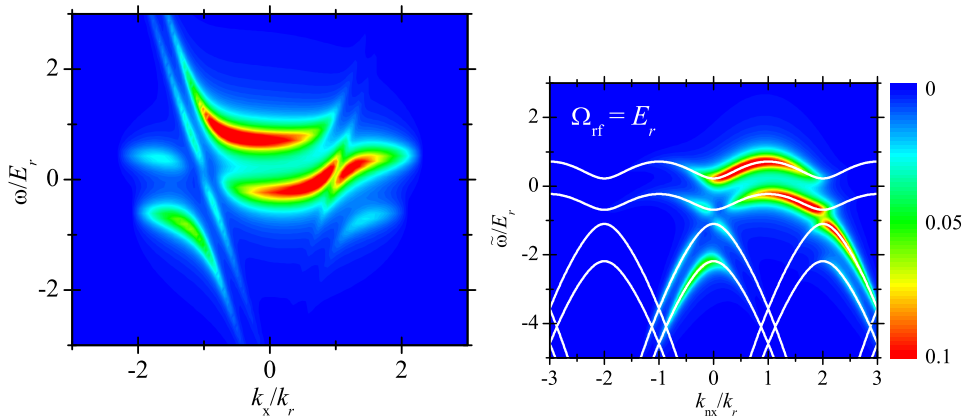

FIG. 4: Theoretical simulation on momentum-resolved rf spectroscopy of a Fermi gas with 1D equal-weight Rashba-Dresselhaus SOC and an additional spin-orbit lattice. The left and right panels show $\Gamma(k_x, \omega)$ and $\Gamma(k_{nx} \equiv k_x + k_r, \tilde{\omega} = \omega + k_x^2/2m)$, respectively. The white lines on the right panel are the calculated energy band structure. The spin-orbit lattice depth is $\Omega_{\rm rf} = E_r$ and the other parameters are the same as in Fig. 3. Figure taken from Ref. [76] with modification.

Experimentally, the single-particle properties of the Fermi gas can also be easily tuned, for example, by using an additional rf field to couple spin-up and down states [12]. After the gauge transformation, it introduces a term $(\Omega/2)[\cos(2k_r x)\hat{\sigma}_x + \sin(2k_r x)\hat{\sigma}_y]$ in the spin-orbit Hamiltonian Eq. (39), which behaves like a spin-orbit lattice and leads to the formation of energy bands. In Fig. 4, we show the simulation of momentum-resolved rf spectroscopy

under such an rf spin-orbit lattice. The energy band structure is apparent. We refer to Ref. [76] for more details on the theoretical simulations, in particular the simulations in a harmonic trap. The relevant measurements will be discussed in greater detail later in the section on experiments.

2. *Two-body physics*

We now turn to consider the interatomic interaction. The interplay between interatomic interaction and SOC can lead to a number of intriguing phenomena, even at the two-particle level. Let us first solve numerically the energy $E(\mathbf{q})$ of the two-particle states by using the general eigenenergy equation Eq. (19). A true bound state must satisfy $E(\mathbf{q}) < 2E_{\min}$, where $E_{\min}$ is the single-particle ground state energy.

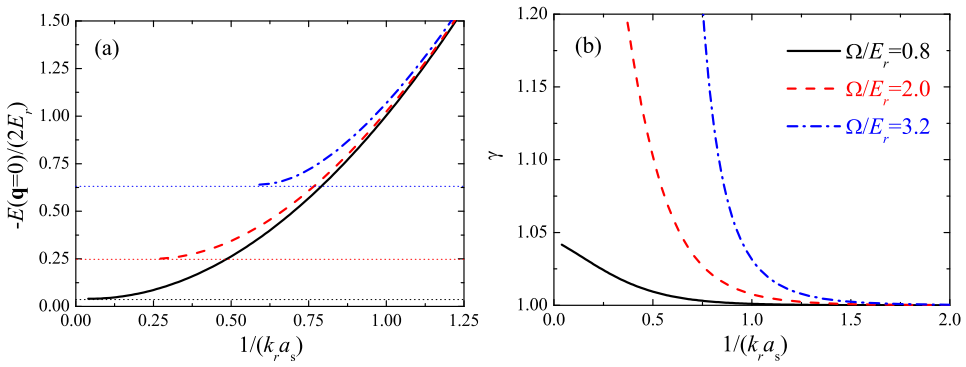

FIG. 5: Energy $-E(q=0)$ (a) and effective mass ratio $\gamma = M_x/(2m)$ (b) of the two-particle ground bound state in the presence of 1D equal-weight Rashba-Dresselhaus SOC, at zero detuning $\delta = 0$ and at three coupling strengths of Raman beams: $\Omega = 0.8E_r$ (solid line), $2E_r$ (dashed line), and $3.2E_r$ (dot-dashed line). The horizontal dotted lines in (a) correspond to the threshold energies $-2E_{\min}$ where the bound states disappear. Figure taken from Ref. [66] with modification.

At zero detuning $\delta = 0$, the two-particle ground state has zero center-of-mass momentum $\mathbf{q} = 0$ [66]. In Fig. 5(a), we show its energy as a function of the dimensionless interaction parameter $1/(k_r a_s)$. In the presence of 1D equal-weight Rashba-Dresselhaus SOC, a two-particle bound state occurs on the BEC side with a positive s-wave scattering length $a_s > 0$. The effective out-of-plane Zeeman field Ω acts as a pair-breaker and pushes the threshold scattering length to the BEC limit. In other words, the position of the Feshbach resonance, originally located at $a_s = \pm\infty$, now shifts to the BEC side with at lower magnetic field strengths [14]. By calculating the dispersion relation $E(\mathbf{q})$ around $\mathbf{q} = 0$, we are able to determine the effective mass, as shown in Fig. 5(b). It is interesting that the effective mass along the direction of SOC is greatly altered. It becomes much larger than $2m$ towards the threshold scattering length. In the deep BEC limit, $1/(k_r a_s) \to \infty$, where two atoms form a tightly bound molecule, the mass is less affected by the SOC or the effective Zeeman field, as we may anticipate.

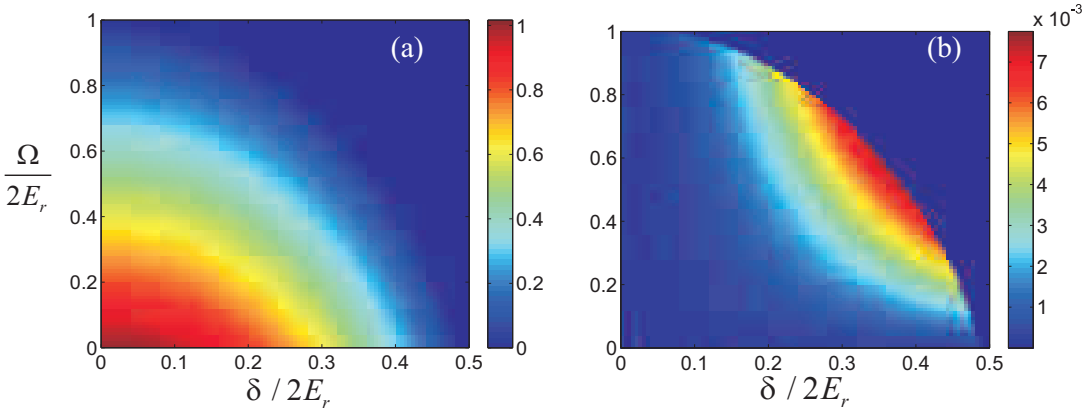

FIG. 6: Binding energy $E_b = 2E_{\min} - E_{\mathbf{q}_0}$ and the magnitude of the lowest-energy bound state momentum q_0 as functions of δ and Ω. The coloring in (a) represents E_b/E_r, and that in (b) represents q_0/k_r. In the upper right corner of both (a) and (b), there exist no bound states. The scattering length is given by $1/(k_r a_s) = 1$. Figure taken from Ref. [26] with modifications.

At nonzero detuning $\delta \neq 0$, the result shows that the two-particle bound state will have its lowest energy at a finite center-of-mass momentum $\mathbf{q}_0 = (q_0, 0, 0)$ [26, 30]. Fig. 6 shows the binding energy and the magnitude of $\mathbf{q}_0$ of the lowest-energy bound state. That the two-particle ground states possessing a finite momentum implies that the Cooper pairs, which is a many-body counterpart of two-particle bound state, may acquire finite center-of-mass momentum and therefore condense into an inhomogeneous superfluid state. This possibility will be addressed in greater detail later. We note that with the typical parameters, i.e., $\Omega \sim E_r$ and $\delta \sim E_r$, q_0 is small and less than 1% of the recoil momentum k_r, as shown in Fig. 6(b). However, its magnitude can be significantly enhanced by many-body effect. For Cooper pairs in the ground state, q_0 can be tuned to be comparable with k_r or the Fermi wavevector k_F [33].

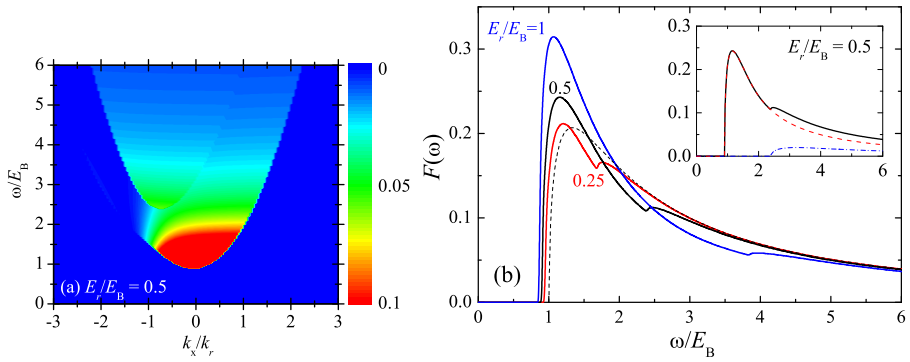

FIG. 7: (a) Momentum-resolved rf spectroscopy (a) and integrated rf spectroscopy (b) of the two-particle bound state at $\delta = 0$ and $\Omega = 2E_r$. The energy of rf photon ω is measured in units of a binding energy $E_B \equiv 1/(ma_s^2)$ and we have set $\omega_{3\downarrow} = 0$. In the right panel, the dashed line in the main figure plots the rf line-shape in the absence of SOC: $F(\omega) = (2/\pi)\sqrt{\omega - E_B}/\omega^2$. The inset highlights the different contribution from the two final states, as described in the text. Figure taken from Ref. [65] with modification.

Ideally, momentum-resolved rf-spectroscopy can be used to probe the two-particle bound state discussed above. We can perform a numerical simulation of the spectroscopy by using again the Fermi's golden rule. Let us assume that a bound molecule is initially at rest in the state $|\Phi_{2B}\rangle$ with energy E_i. An rf photon with energy ω will break the molecule and transfer the spin-down atom to the third state $|3\rangle$. In the case that there is no final-state effect, the final state $|\Phi_f\rangle$ consists of a free atom in $|3\rangle$ and a remaining atom in the spin-orbit system. According to the Fermi's golden rule, the rf strength $\Gamma(\omega)$ of breaking molecules and transferring atoms is proportional to the Franck-Condon factor [77],

$$F(\omega) = |\langle \Phi_f | \mathcal{V}_{rf} | \Phi_{2B} \rangle|^2 \, \delta\left[\omega - \omega_{3\downarrow} - (E_f - E_i)\right]. \tag{43}$$

The integrated Franck-Condon factor satisfies the sum rule, $\int_{-\infty}^{+\infty} F(\omega)\, d\omega = 1$. A closed expression of $F(\omega)$ is derived in Refs. [65] and [66], by carefully analyzing the initial two-particle bound state $|\Phi_{2B}\rangle$ and the final state $|\Phi_f\rangle$. Furthermore, by resolving the momentum of transferred atoms, we are able to obtain the momentum-resolved Franck-Condon factor $F(k_x, \omega)$.

Figs. 7(a) and 7(b) illustrate respectively the momentum-resolved and the integrated rf spectrum of the two-particle ground state at zero detuning $\delta = 0$. One can easily resolve two different responses in the spectrum due to two different final states, as the remaining spin-up atom in the original spin-orbit system can occupy either the upper or the lower energy branch. Indeed, in the integrated rf spectrum, we can separate clearly the different contributions from the two final states, as highlighted in the inset. This gives rise to two peaks in the integrated spectrum. We note that the lower peak exhibits a red shift as the SOC strength increases, due to the decrease of the binding energy. It is also straightforward to calculate the rf spectrum of the two-particle bound state at nonzero detuning $\delta \neq 0$ (not shown in the figure). However, the spectrum remains essentially unchanged, due to the fact that the center-of-mass momentum q_0 is quite small with typical experimental parameters.

3. Momentum-resolved radio-frequency spectrum of the superfluid phase

Consider now the many-body state. As we mentioned earlier, since the two-particle wave function contains both spin singlet and triplet components, we anticipate that the superfluid phase at low temperatures would involve both s-wave pairing and high-partial-wave pairing. Therefore, in general it is an anisotropic superfluid. This is to be discussed later in detail for 2D Rashba SOC. Here, we are interested in the phase diagram and the experimental probe

of a 3D Fermi gas with 1D equal-weight Rashba-Dresselhaus SOC. First, let us concentrate on the case with zero detuning $\delta = 0$, by using the many-body T-matrix theory within the pseudogap approximation [13].

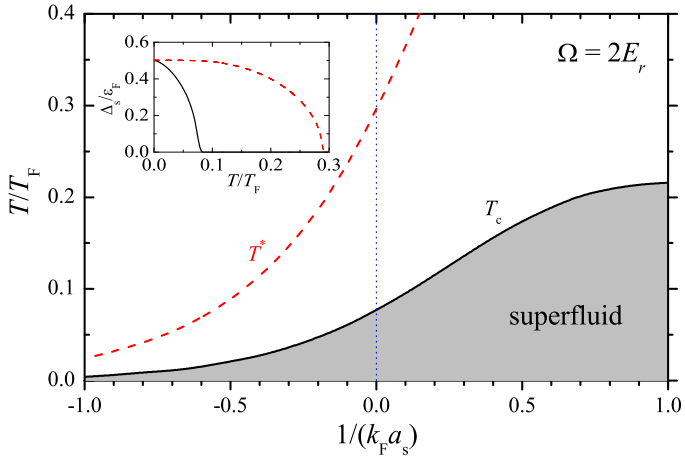

FIG. 8: (a) Phase diagram of a spin-orbit coupled Fermi gas at the BEC-BCS crossover at $\Omega = 2E_r$ and $k_F = k_r$. The main figure and inset show the superfluid transition temperature and the superfluid order parameter at resonance, respectively, predicted by using our T-matrix theory (solid line) and the BCS mean-field theory (dashed line). Figure taken from Ref. [13] with modification.

Focusing on the vicinity of the Feshbach resonance where $a_s \to \pm\infty$, in Fig. 8 we show the superfluid transition temperature T_c and the pair breaking (pseudogap) temperature T^* of the spin-orbit coupled Fermi gas at $\Omega = 2E_r$ and $k_F = k_r$. The pseudogap temperature is calculated using the standard BCS mean-field theory without taking into account the preformed pairs (i.e., $\Delta_{pg} = 0$) [57, 67]. We find that the region of superfluid phase is strongly suppressed by SOC. In particular, at resonance the superfluid transition temperature is about $T_c \simeq 0.08T_F$, which is significantly smaller than the experimentally determined $T_c \simeq 0.167(13)T_F$ for a unitary Fermi gas [78]. Thus, it seems to be a challenge to observe a novel spin-orbit coupled fermionic superfluid in the present experimental scheme.

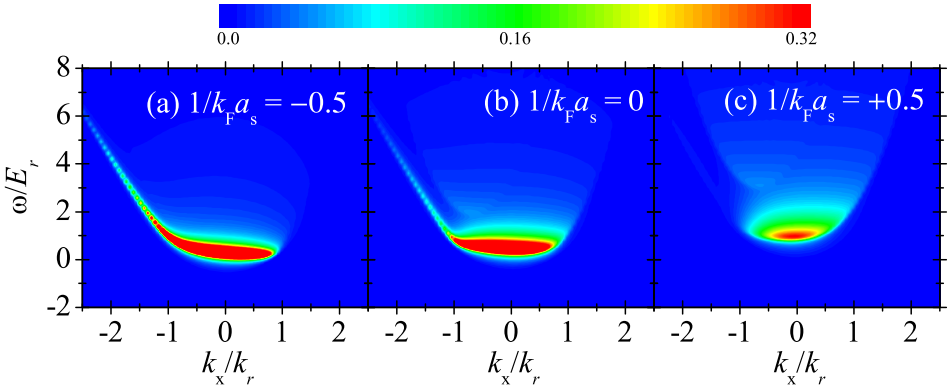

FIG. 9: Zero-temperature momentum-resolved rf-spectroscopy of a spin-orbit coupled Fermi gas across the Feshbach resonance, at the parameters $\Omega = 2E_r$ and $k_F = k_r$. Figure taken from Ref. [13] with modification.

In Figs. 9(a)-9(c), we show the zero-temperature momentum-resolved rf spectrum across the resonance. On the BCS side ($1/k_F a_s = -0.5$), the spectrum is dominated by the response from atoms and shows a characteristic high-frequency tail at $k_x < 0$ [11, 12, 76], see for example, the left panel of Fig. 3. We note that the density of the Fermi cloud, chosen here following the real experimental parameters [11], is low and therefore only the lower energy branch is occupied at low temperatures. Towards the BEC limit ($1/k_F a_s = +0.5$), the spectrum may be understood from the picture of well-defined bound pairs and shows a clear two-fold anisotropic distribution, as we already mentioned in Fig. 7(a) [65]. The spectrum at the resonance is complicated and might be attributed to many-body fermionic pairs. It is interesting that the response from many-body pairs has a similar tail at high frequency as that from atoms. The change of the rf spectrum across the resonance is continuous, in accordance with a smooth BEC-BCS crossover.

4. Fulde-Ferrell superfluidity

The nature of superfluidity can be greatly changed by a nonzero detuning $\delta \neq 0$. As we discussed earlier in the two-body part, in this case, the Cooper pairs may carry a nonzero center-of-mass momentum and therefore condense into an inhomogeneous superfluid state, characterized by the order parameter $\Delta_0(\mathbf{r}) = \Delta_0 e^{i\mathbf{q}\cdot\mathbf{r}}$. This exotic superfluid has been proposed by Fulde and Ferrell [63], soon after the discovery of the seminal BCS theory. Its existence has attracted tremendous theoretical and experimental efforts over the past five decades [79]. Remarkably, to date there is still no conclusive experimental evidence for FF superfluidity. Here, we show that the superfluid phase of a 3D Fermi gas with 1D equal-weight Rashba-Dresselhaus SOC and finite in-plane effective Zeeman field δ is precisely the long-sought FF superfluid [33]. The same issue has also been addressed very recently by Vijay Shenoy [30]. We note that the FF superfluid can appear in other settings with different types of SOC and dimensionality [29, 31, 32, 34–36, 80].

Theoretically, to determine the FF superfluid state, we solve the BdG equation (29) with $V_T(\mathbf{r}) = 0$ by using the following ansatz for quasiparticle wave functions

$$\Phi_{\mathbf{k}\eta}(\mathbf{x}) = \frac{e^{i\mathbf{k}\cdot\mathbf{x}}}{\sqrt{V}}\left[u_{\mathbf{k}\eta\uparrow}e^{+iqx/2}, u_{\mathbf{k}\eta\downarrow}e^{+iqx/2}, v_{\mathbf{k}\eta\uparrow}e^{-iqx/2}, v_{\mathbf{k}\eta\downarrow}e^{-iqx/2}\right]^T. \tag{44}$$

The center-of-mass momentum $\mathbf{q}$ is assumed to be along the x-direction, inspired from the two-body solution [26]. The mean-field thermodynamic potential Ω_0 at temperature T in Eq. (10) is then given by

$$\frac{\Omega_0}{V} = \frac{1}{2V}\left[\sum_{\mathbf{k}}\left(\xi_{\mathbf{k}+\mathbf{q}/2} + \xi_{\mathbf{k}-\mathbf{q}/2}\right) - \sum_{\mathbf{k}\eta} E_{\mathbf{k}\eta}\right] - \frac{k_B T}{V}\sum_{\mathbf{k}\eta}\ln\left(1 + e^{-E_{\mathbf{k}\eta}/k_B T}\right) - \frac{\Delta_0^2}{U_0}, \tag{45}$$

where $E_{\mathbf{k}\eta}$ ($\eta = 1, 2, 3, 4$) is the quasiparticle energy. Here, the summation over the quasiparticle energy must be restricted to $E_{\mathbf{k}\eta} \geq 0$ because of an inherent particle-hole symmetry in the Nambu spinor representation. For a given set of parameters (i.e, the temperature T, interaction strength $1/k_F a_s$, etc.), different mean-field phases can be determined using the self-consistent stationary conditions: $\partial\Omega/\partial\Delta = 0$, $\partial\Omega/\partial q = 0$, as well as the conservation of total atom number, $N = -\partial\Omega/\partial\mu$. At finite temperatures, the ground state has the lowest free energy $F = \Omega + \mu N$. In the following, we consider the resonance case with a divergent scattering length $1/k_F a_s = 0$ and set $T = 0.05T_F$, where T_F is the Fermi temperature. According to the typical number of atoms in experiments [11, 12], we take the Fermi wavevector $k_F = k_r$.

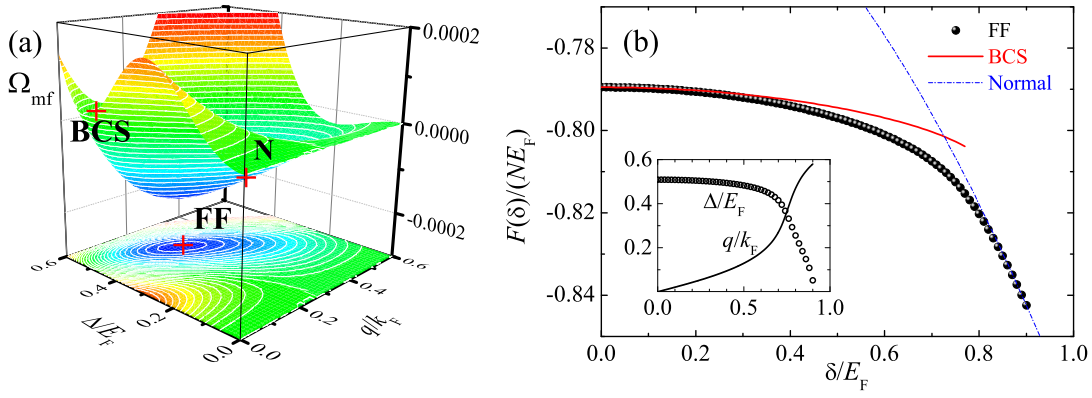

FIG. 10: (a) Landscape of the thermodynamic potential, $\Omega_{\rm mf} = [\Omega_0(\Delta, q) - \Omega_0(0, 0)]/(NE_F)$, at $\Omega = 2E_F$ and $\delta = 0.68E_F$. The chemical potential is fixed to $\mu = -0.471E_F$. The competing ground states include (i) a normal Fermi gas with $\Delta_0 = 0$; (ii) a fully paired BCS superfluid with $\Delta_0 \neq 0$ and $q = 0$; and (iii) a finite momentum paired FF superfluid with $\Delta_0 \neq 0$ and $q \neq 0$. (b) The free energy of different competing states as a function of the detuning at $\Omega = 2E_F$. The inset shows the detuning dependence of the order parameter and momentum of the FF superfluid state. Figure taken from Ref. [33] with modification.

In general, for any set of parameters there are three competing ground states that are stable against phase separation (i.e., $\partial^2\Omega_0/\partial\Delta_0^2 \geq 0$), as shown in Fig. 10(a): normal gas ($\Delta_0 = 0$), BCS superfluid ($\Delta_0 \neq 0$ and $q = 0$), and FF superfluid ($\Delta_0 \neq 0$ and $q \neq 0$). Remarkably, in the presence of spin-orbit coupling the FF superfluid is always more favorable in energy than the standard BCS pairing state at finite detuning (Fig. 10(b)). It is easy to check that the superfluid density of the BCS pairing state in the SOC direction becomes negative (i.e., $\partial\Omega_0/\partial q < 0$), signaling the instability towards an FF superfluid. Therefore, experimentally the Fermi gas would always condense into an

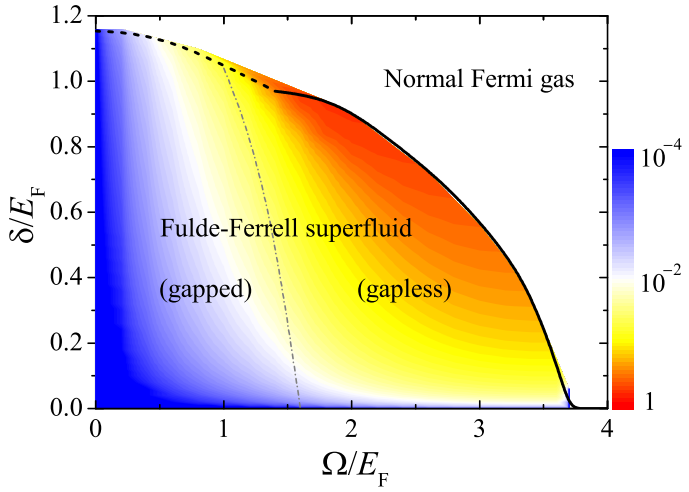

FIG. 11: Phase diagram as a function of δ and Ω, at $T = 0.05T_F$. By increasing δ, the Fermi cloud changes from a FF superfluid to a normal gas, via first-order (dashed line) and second-order (solid line) transitions at low and high Ω, respectively. The FF superfluid can be either gapped or gapless, as separated by the dot-dashed line. The coloring represents the magnitude of the centre-of-mass momentum of Cooper pairs, q/k_F. The BCS superfluid occurs at $\Omega = 0$ or $\delta = 0$ only. Figure taken from Ref. [33] with modification.

FF superfluid at finite two-photon detuning. In Fig. 11, we report a low-temperature phase diagram that could be directly observed in current experiments. The FF superfluid occupies the major part of the phase diagram.

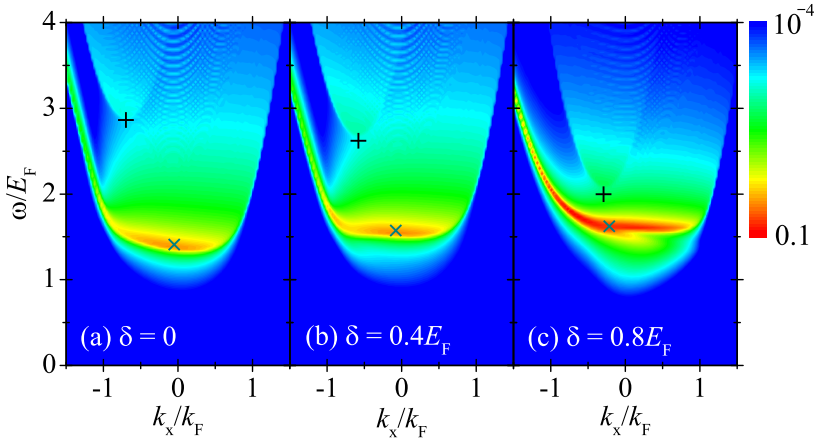

FIG. 12: Logarithmic contour plot of momentum-resolved rf spectroscopy: number of transferred atoms $\Gamma(k_x, \omega)$ at $\Omega = 2E_F$ and at three detunings: (a) $\delta = 0$ and $q = 0$, (b) $\delta = 0.4E_F$ and $q \simeq 0.1k_F$, and (c) $\delta = 0.8E$ and $q \simeq 0.6k_F$. Figure taken from Ref. [33] with modification.

The experimental probe of an FF superfluid is a long-standing challenge. Here, unique to cold atoms, momentum-resolved rf spectroscopy may provide a smoking-gun signal of the FF superfluidity. The basic idea is that, since Cooper pairs carry a finite center-of-mass momentum $\mathbf{q}$, the transferred atoms in the rf transition acquire an overall momentum $\mathbf{q}/2$. As a result, there would be a $\mathbf{q}/2$ shift in the measured spectrum. In Fig. 12, we show the momentum-resolved rf spectrum $\Gamma(k_x, \omega)$ on a logarithmic scale. As we discussed earlier in the two-body part, there are two contributions to the spectrum, corresponding to two different final states [65]. These two contributions are well separated in the frequency domain, with peak positions indicated by the symbols "+" and "×", respectively. Interestingly, at finite detuning with a sizable FF momentum $\mathbf{q}$, the peak positions of the two contributions are shifted roughly in opposite directions by an amount $\mathbf{q}/2$. This provides clear evidence for observing the FF superfluid.

5. 1D topological superfluidity

Arguably, the most remarkable aspect of SOC is that it provides a feasible routine to realize topological superfluids [38], which have attracted tremendous interest over the past few years [81]. In addition to providing a new quantum phase of matter, topological superfluids can host exotic quasiparticles at their boundaries, known as Majorana fermions - particles that are their own antiparticles [82, 83]. Due to their non-Abelian exchange statistics, Majorana fermions are believed to be the essential quantum bits for topological quantum computation [84]. Therefore, the pursuit for topological superfluids and Majorana fermions represents one of the most important challenges in fundamental science. A number of settings have been proposed for the realization of topological superfluids, including the fractional quantum Hall states at filling $\nu = 5/2$ [85], vortex states of $p_x + ip_y$ superconductors [86, 87], and surfaces of three-dimensional (3D) topological insulators in proximity to an s-wave superconductor [88], and one-dimensional (1D) nanowires with strong spin-orbit coupling coated also on an s-wave superconductor [89]. In the latter setting, indirect evidences of topological superfluid and Majorana fermions have been reported [90]. Here, we review briefly the possible realizations of topological superfluids, in the context of a 1D spin-orbit coupled atomic Fermi gas [45, 47, 51, 55], which can be prepared straightforwardly by loading a 3D spin-orbit Fermi gas into deep 2D optical lattices. Later, we will discuss 2D topological superfluids with Rashba SOC.

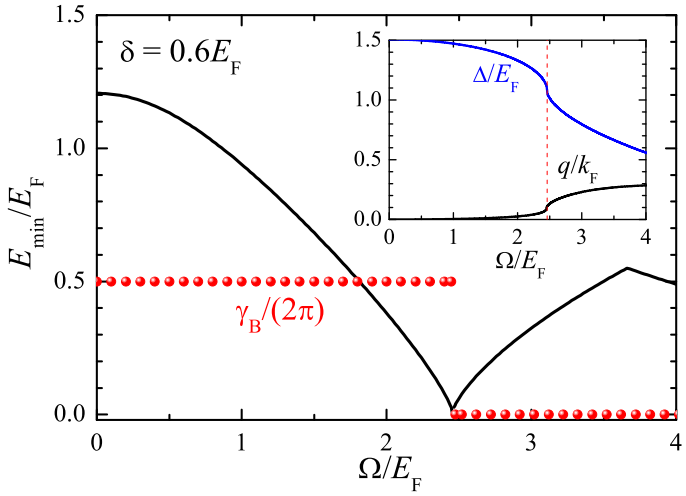

FIG. 13: Theoretical examination of the topological phase transition at the detuning $\delta = 0.6E_F$ and $T = 0$. The transition occurs at $\Omega \simeq 2.46E_F$, where the energy gap of the system (solid line) close and then open. The Berry phase γ_B is π and 0 at the topologically trivial and non-trivial regimes (circles). The insets shows the order parameter and momentum of the FF superfluid, as a function of the Rabi frequency. Figure taken from Ref. [55] with modification.

Consider first a homogeneous 1D Fermi gas with a nonzero detuning $\delta \neq 0$ [55]. In this case, we actually anticipate a topological inhomogeneous superfluid, where the order parameter also varies in real space. Using the same theoretical technique as in the previous subsection, we solve the BdG equation (29) in 1D and then minimize the mean-field thermodynamic potential Eq. (45) to determine the pairing gap Δ_0 and the FF momentum q.

In Fig. 13, we show the energy gap as a function of Ω at $\delta = 0.6E_F$ and $T = 0$. For this result, we use a Fermi wavevector $k_F = 0.8k_r$ and take a dimensionless interaction parameter $\gamma \equiv -mg_{1D}/(n) = 3$, where g_{1D} is the strength of the 1D contact interaction and $n = 2k_F/\pi$ is the 1D linear density. Topological phase transition is associated with a change of the topology of the underlying Fermi surface and therefore is accompanied with closing of the excitation gap at the transition point. In the main figure this feature is clearly evident. To better characterize the change of topology, we may calculate the Berry phase defined by [47]

$$\gamma_B = i \int_{-\infty}^{+\infty} dk \left[W_+^*(k)\partial_k W_+(k) + W_-^*(k)\partial_k W_-(k) \right]. \tag{46}$$

Here $W_\eta(k) \equiv [u_{k\eta\uparrow}e^{iqz/2}, u_{k\eta\downarrow}e^{iqz/2}, v_{k\eta\uparrow}e^{-iqz/2}, v_{k\eta\downarrow}e^{-iqz/2}]^T$ denotes the wave function of the upper ($\eta = +$) and lower ($\eta = -$) branch, respectively. In Fig. 13, the Berry phase is shown by circles. It jumps from π to 0, right across the topological phase transition. It is somewhat counter-intuitive that the $\gamma_B = 0$ sector corresponds to the topologically non-trivial superfluid state. It is important to emphasize the inhomogeneous nature of the superfluid.

Indeed, as shown in the inset, the FF momentum q increases rapidly across the topological superfluid transition and reaches about $0.3k_F$ at $\Omega = 4E_F$.

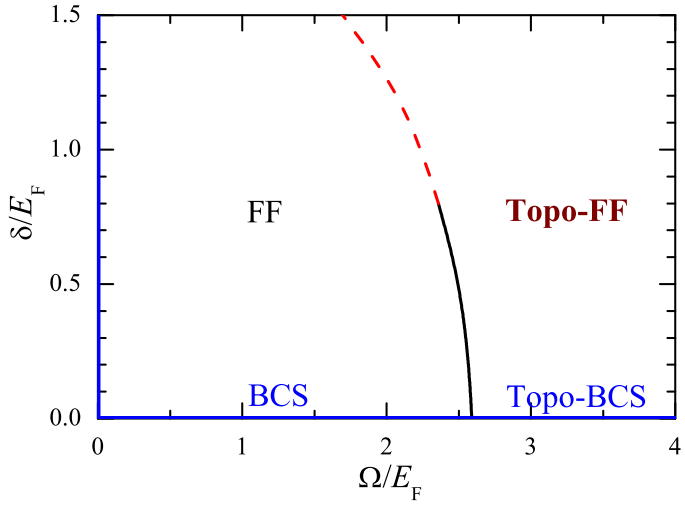

FIG. 14: Zero-temperature phase diagram. A topologically non-trivial FF superfluid appears when the Raman coupling strength Ω is above a threshold at finite detunings δ. Depending on the detuning, the transition could be either continuous (solid line) or of first order (dashed line). The FF superfluid reduces to a BCS superfluid when $\Omega = 0$ or $\delta = 0$. Figure taken from Ref. [55] with modification.

In Fig. 14, we present the zero-temperature phase diagram for the topological phase transition. The critical coupling strength Ω_c decreases with the increase of the detuning δ. At zero detuning, Ω_c can be determined analytically, since the expression for the BdG eigenenergy for single-particle excitations (after dropping a constant energy shift E_r) is known [24, 47],

$$E_{k\eta} = \left[\left(\xi_k^2 + \lambda^2 k^2 + \Omega^2/4 + \Delta_0^2 \pm \sqrt{4\xi_k^2\lambda^2 k^2 + \Omega^2\left(\xi_k^2 + \Delta_0^2\right)}\right)\right]^{1/2}, \tag{47}$$

where $\xi_k = k^2/(2m) - \mu$ and $\lambda = k_r/m$. It is easy to see that the excitation gap closes at $k = 0$ for the lower branch (i.e., $\eta = -$), leading to the well-known result [89]

$$\frac{\Omega_c}{2} = \sqrt{\mu^2 + \Delta^2}. \tag{48}$$

This criterion for topological superfluids is equivalent to the condition that there are only two Fermi points on the Fermi surface [39], under which the Fermi system behaves essentially like a 1D weak-coupling p-wave superfluid.

Let us now turn to the experimentally realistic situation with a 1D harmonic trap $V_T(x) = m\omega^2 x^2/2$ and focus on the case with $\delta = 0$ [45, 47, 51]. The BdG equation (29) can be solved self-consistently by expanding the Nambu spinor wave function $\Phi_\eta(x)$ onto the eigenfucntion basis of the harmonic oscillator. In this trapped environment, Majorana fermions with zero energy are anticipated to emerge at the boundary, if the Fermi gas stays in a topological superfluid state. The appearance of Majorana fermions can be easily understood from the particle-hole symmetry obeyed by the BdG equation, which states that every physical state can be described either by a particle state with a positive energy E or a hole state with a negative energy $-E$. The Bogoliubov quasiparticle operators associated with these two states therefore satisfy $\Gamma_E = \Gamma^\dagger_{-E}$. At the boundary, Eq. (48) could be fulfilled at some points and give locally the states with $E = 0$. These states are Majorana fermions, as the associated operators satisfy $\Gamma_0 = \Gamma_0^\dagger$ - precisely the defining feature of a Majorana fermion [82, 83].

In Fig. 15(a), we present the zero-temperature phase diagram of a trapped 1D Fermi gas at $k_F = 2k_r$ and $\gamma = \pi$ [51]. The transition from BCS superfluid to topological superfluid is now characterized by the appearance of Majorana fermions, whose energy is precisely zero and therefore the minimum of the quaisparticle spectrum touches zero, $\min\{|E_\eta|\} = 0$. In the topological superfluid phase, as shown in Fig. 15(b) with $\Omega = 2.4E_F$, the Majorana fermions may be clearly identified by using spatially-resolved rf spectroscopy. We note that for a trapped Fermi gas with weak interatomic interaction and/or high density, the upper branch of single-particle spectrum may be populated at the trap center, leading to four Fermi points on the Fermi surface. This violates Eq. (48). As a result, we may find a phase-separation phase in which the topological superfluid occurs only at the two wings of the Fermi cloud. This situation has been discussed in Ref. [45].

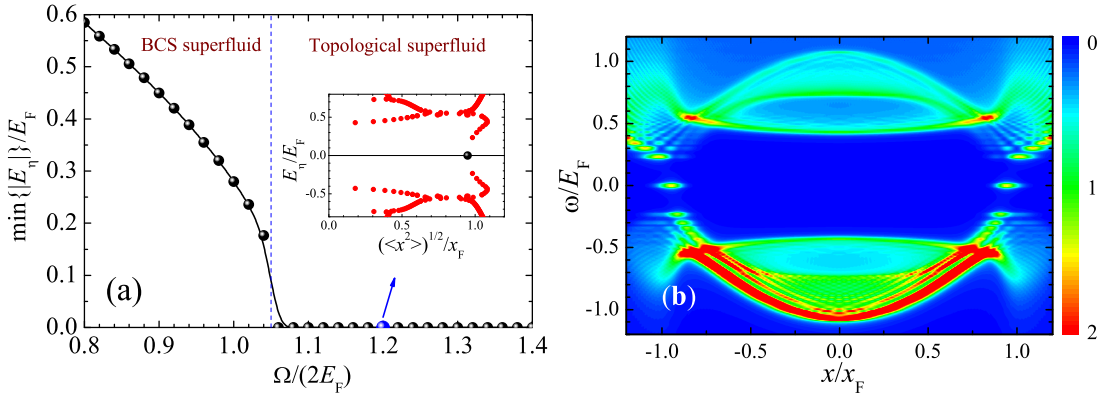

FIG. 15: (a) Zero-temperature phase diagram of a trapped 1D spin-orbit coupled Fermi gas, determined from the behavior of the lowest energy in quasiparticle spectrum. The inset shows the energy spectrum at $\Omega = 2.4E_F$ as a function of the position of quasiparticles. A zero-energy quasiparticle (i.e., Majorana fermion) at the trap edge has been highlighted by a big dark circle. Here, the position of a quasiparticle is approximately characterized by: $\langle x^2 \rangle = \int dx x^2 \sum_\sigma [u_\sigma^2(x) + \nu_\sigma^2(x)]$. x_F is the Thomas-Fermi radius of the cloud. (b) Linear contour plot of the local density of state at $\Omega = 2.4E_F$. At each trap edge, a series of edge states, including the zero-energy Majorana fermion mode, are clearly visible. Figure taken from Ref. [51] with modification.

C. 2D Rashba spin-orbit coupling

Let us now discuss Rashba SOC, which takes the standard form $V_{\rm SO} = \lambda(\hat{k}_y\hat{\sigma}_x - \hat{k}_x\hat{\sigma}_y)$ [91]. The coupling between spin and orbital motions occurs along two spatial directions and therefore we shall refer to it as 2D Rashba SOC. This type of SOC is not realized experimentally yet, although there are several theoretical proposals for its realization [92, 93]. The superfluid phase with 2D Rashba SOC at low temperatures shares a lot of common features as its 1D counterpart as we reviewed in the previous subsection. Here we focus on some specific features, for example, the two-particle bound state at sufficiently strong SOC strength - the rashbon [21, 25] - and the related crossover to a BEC of rashbons. We will also discuss in greater detail the 2D topological superfluid with Rasbha SOC in the presence of an out-of-plane Zeeman field, since it provides an interesting platform to perform topological quantum computation. We note that experimentally it is also possible to create a 3D isotropic SOC, $V_{\rm SO} = \lambda(\hat{k}_x\hat{\sigma}_x + \hat{k}_y\hat{\sigma}_y + \hat{k}_z\hat{\sigma}_z)$, where the spin and orbital degree of freedoms are coupled in all three dimensions [94]. We note also that early theoretical works on a Rashba spin-orbit coupled Fermi gas was reviewed very briefly by Hui Zhai in Ref. [95].

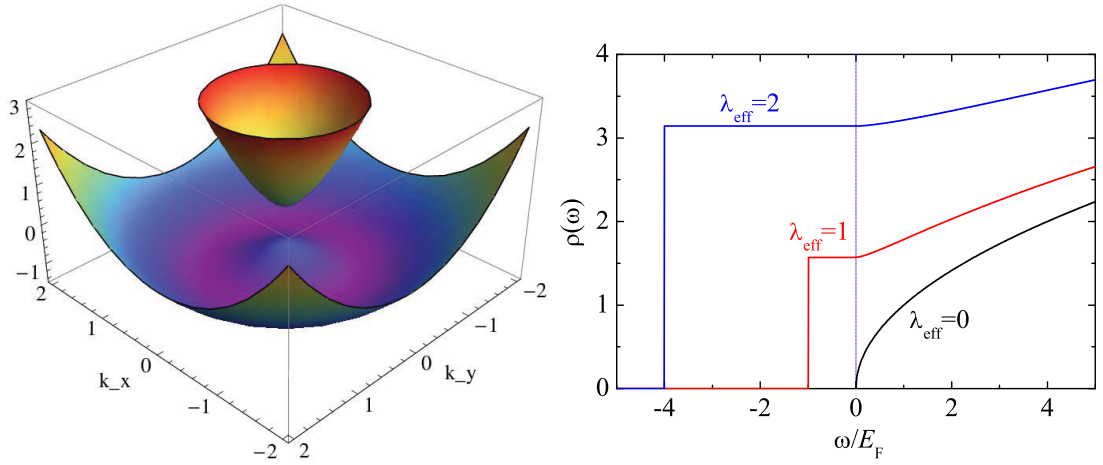

FIG. 16: Left panel: schematic of the single-particle spectrum in the $k_x - k_y$ plane. A energy gap opens at $k = 0$, due to a nonzero out-of-plane Zeeman field h. Right panel: density of states of a 3D homogeneous Rashba spin-orbit coupled system at several SOC strengths, in units of mk_F. Right figure taken from Ref. [96] with modification.

1. Single-particle spectrum

In the presence of an out-of-plane Zeeman field $h\hat{\sigma}_z$, the single-particle spectrum is given by,

$$E_{\mathbf{k}\pm} = \frac{\mathbf{k}^2}{2m} \pm \sqrt{\lambda^2\left(k_x^2+k_y^2\right)+h^2}\,. \tag{49}$$

The spectrum with a nonzero h is illustrated on the left panel of Fig. 16. Compared with the single-particle spectrum with 1D equal-weight Rashba-Dresselhaus SOC in Fig. 2, it is interesting that the two minima in the lower energy branch now extend to form a ring structure. At low energy, therefore, we may anticipate that in the momentum space the particles will be confined along the ring. The effective dimensionality of the system is therefore reduced. Indeed, it is not difficult to obtain the density of states ($h=0$) [96]:

$$\rho\left(\omega\right) = \left(mk_F\right)\begin{cases} 0, & \left(\omega < -\lambda_{\text{eff}}^2\right); \\ \lambda_{\text{eff}}\pi/2, & \left(-\lambda_{\text{eff}}^2 \leq \omega < 0\right); \\ \sqrt{\omega/E_F}+\lambda_{\text{eff}}\left[\pi/2-\arctan\sqrt{\omega/\left(\lambda_{\text{eff}}^2 E_F\right)}\right], & \left(\omega \geq 0\right). \end{cases}, \tag{50}$$

where we have defined a dimensionless SOC coupling strength $\lambda_{\text{eff}} \equiv m\lambda/k_F$. As can be seen from the right panel of Fig. 16, $\rho(\omega)$ with Rashba SOC becomes a constant at low energy, which is characteristic of a 2D system. This reduction in the effective dimensionality will have interesting consequences when the interatomic interaction comes into play, as we now disucss in greater detail.

2. Two-body physics

We solve the two-body problem by calculating the two-particle vertex function, following the general procedure outlined in the theoretical framework (Sec. II A). Focusing on the case without Zeeman fields, we have

$$\mathcal{G}_0\left(K\right) = \frac{\left(i\omega_m-\xi_{\mathbf{k}}\right)+\lambda\left(k_y\sigma_x-k_x\sigma_y\right)}{\left(i\omega_m-\xi_{\mathbf{k}}\right)^2-\lambda^2\left(k_x^2+k_y^2\right)}. \tag{51}$$

By substituting it into Eq. (16), it is straightforward to obtain,

$$\Gamma^{-1} = \frac{1}{U_0}+\frac{k_BT}{V}\sum_{\mathbf{k},i\omega_m}\left[\frac{1/2}{\left(i\omega_m-E_{\mathbf{k},+}\right)\left(i\nu_n-i\omega_m-E_{\mathbf{q}-\mathbf{k},+}\right)}+\frac{1/2}{\left(i\omega_m-E_{\mathbf{k},-}\right)\left(i\nu_n-i\omega_m-E_{\mathbf{q}-\mathbf{k},-}\right)}-A_{res}\right], \tag{52}$$

with the single-particle energy

$$E_{\mathbf{k},\pm} \;=\; \xi_{\mathbf{k}} \pm \lambda\sqrt{k_x^2+k_y^2}, \tag{53}$$

and

$$A_{res} \equiv \frac{\lambda^2 k_\perp\sqrt{\left(q_x-k_x\right)^2+\left(q_y-k_y\right)^2}+\lambda^2 k_x\left(q_x-k_x\right)+\lambda^2 k_y\left(q_y-k_y\right)}{\left(i\omega_m-E_{\mathbf{k},+}\right)\left(i\omega_m-E_{\mathbf{k},-}\right)\left(i\nu_n-i\omega_m-E_{\mathbf{q}-\mathbf{k},+}\right)\left(i\nu_n-i\omega_m-E_{\mathbf{q}-\mathbf{k},-}\right)}. \tag{54}$$

By performing explicitly the summation over $i\omega_m$, replacing $\mathbf{k}$ by $\mathbf{q}/2+\mathbf{k}$ and re-arranging the terms, we find that

$$\begin{aligned}\Gamma^{-1} \;=\; & \frac{m}{4\pi a_s}+\frac{1}{2V}\sum_{\mathbf{k}}\left[\frac{f\left(E_{\mathbf{q}/2+\mathbf{k},+}\right)+f\left(E_{\mathbf{q}/2-\mathbf{k},+}\right)-1}{i\nu_n-E_{\mathbf{q}/2+\mathbf{k},+}-E_{\mathbf{q}/2-\mathbf{k},+}}+\frac{f\left(E_{\mathbf{q}/2+\mathbf{k},-}\right)+f\left(E_{\mathbf{q}/2-\mathbf{k},-}\right)-1}{i\nu_n-E_{\mathbf{q}/2+\mathbf{k},-}-E_{\mathbf{q}/2-\mathbf{k},-}}-\frac{1}{\epsilon_{\mathbf{k}}}\right] \\ & -\frac{1}{4V}\sum_{\mathbf{k}}\left[1+\frac{q_\perp^2/4-k_\perp^2}{\sqrt{\left(q_x/2+k_x\right)^2+\left(q_y/2+k_y\right)^2}\sqrt{\left(q_x/2-k_x\right)^2+\left(q_y/2-k_y\right)^2}}\right]C_{res},\end{aligned} \tag{55}$$

where

$$\begin{aligned}C_{res} \;=\; & +\frac{\left[f\left(E_{\mathbf{q}/2+\mathbf{k},+}\right)+f\left(E_{\mathbf{q}/2-\mathbf{k},+}\right)-1\right]}{i\nu_n-E_{\mathbf{q}/2+\mathbf{k},+}-E_{\mathbf{q}/2-\mathbf{k},+}}+\frac{\left[f\left(E_{\mathbf{q}/2+\mathbf{k},-}\right)+f\left(E_{\mathbf{q}/2-\mathbf{k},-}\right)-1\right]}{i\nu_n-E_{\mathbf{q}/2+\mathbf{k},-}-E_{\mathbf{q}/2-\mathbf{k},-}} \\ & -\frac{\left[f\left(E_{\mathbf{q}/2+\mathbf{k},+}\right)+f\left(E_{\mathbf{q}/2-\mathbf{k},-}\right)-1\right]}{i\nu_n-E_{\mathbf{q}/2+\mathbf{k},+}-E_{\mathbf{q}/2-\mathbf{k},-}}-\frac{\left[f\left(E_{\mathbf{q}/2+\mathbf{k},-}\right)+f\left(E_{\mathbf{q}/2-\mathbf{k},+}\right)-1\right]}{i\nu_n-E_{\mathbf{q}/2+\mathbf{k},-}-E_{\mathbf{q}/2-\mathbf{k},+}}.\end{aligned} \tag{56}$$

The above equation provides a starting point to investigate the fluctuation effect due to interatomic interactions.

Here, for the two-body problem of interest, we discard the Fermi distribution function and set $\mathbf{q}=0$, as the ground bound state has zero center-of-mass momentum in the absence of Zeeman field. The two-body vertex function is then given by,

$$\Gamma_{2\mathrm{b}}^{-1}\left(\mathbf{q}=\mathbf{0};i\nu_n\to\omega+i0^+\right)=\frac{m}{4\pi a_s}-\frac{1}{2V}\sum_{\mathbf{k}}\left[\frac{1}{\omega+i0^+-2E_{\mathbf{k},+}}+\frac{1}{\omega+i0^+-2E_{k,-}}+\frac{1}{\epsilon_{\mathbf{k}}}\right], \tag{57}$$

The energy of the two-particle bound state E can be obtained by solving $\mathrm{Re}\{\Gamma_{2\mathrm{b}}^{-1}\left[\mathbf{q}=\mathbf{0};\omega=E\right]\}=0$ with $\mu=0$, as we already discussed in the theoretical framework. More physically, we may calculate the phase shift

$$\delta_{2\mathrm{b}}\left(\mathbf{q}=\mathbf{0};\omega\right)=-\mathrm{Im}\ln\left[-\Gamma_{2\mathrm{b}}^{-1}\left(\mathbf{q}=\mathbf{0};i\nu_n\to\omega+i0^+\right)\right]. \tag{58}$$

Recall that the vertex function represents the Green function of Cooper pairs. Thus, the phase shift defined above is simply $\int d\omega A(\mathbf{q},\omega)$, where $A(\mathbf{q},\omega)$ is the spectral function of pairs. As a result, a true bound state, corresponding to a delta peak in the spectral function, will cause a π jump in the phase shift at the critical frequency $\omega_c=E$, from which we determine the energy of the bound state.

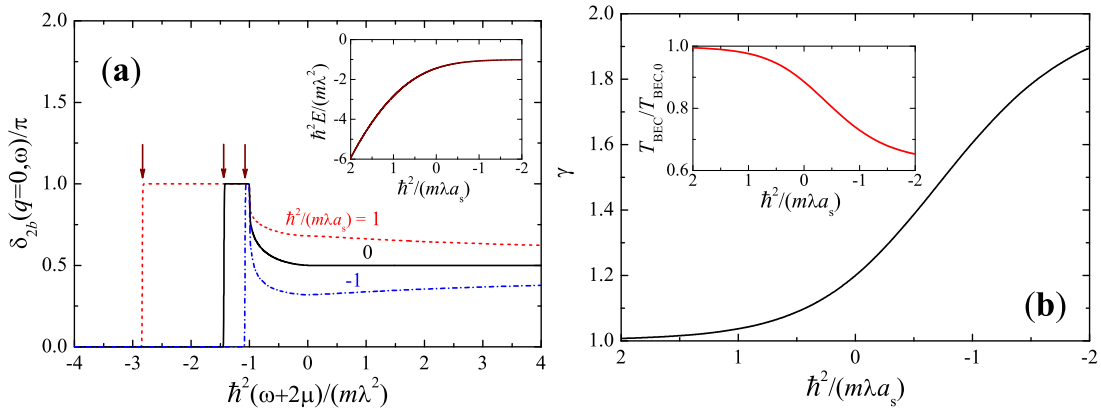

FIG. 17: (a) Two-body bound states as evidenced by the two-body phase shift at three different scattering lengths, in the presence of Rashba SOC. The arrows indicate the position of the bound state energy. The inset shows the bound state energy as a function of the scattering length. (b) Effective mass of the two-body bound state. The inset shows the decreases of critical temperature due to the heavy mass of bound states. Figure taken from Ref. [22] with modification.

In the main figure and inset of Fig. 17(a), we show the two-body phase shift and the energy of the bound state of a Rashba spin-orbit coupled Fermi gas, respectively. Interestingly, the bound state exists even in the BCS limit, where the s-wave scattering length is small and negative [20]. This is because at the low energy the effective dimensionality of the Rashba system reduces to two, as we mentioned earlier from the nature of the low-energy density of states. In 2D, we know that any weak attraction can lead to a bound state. We can calculate the effective mass of the bound state [22, 23], which is strongly renormalized by the SOC, by determining the dispersion relation of the two-body bound state $E(\mathbf{q})$ at small momentum $\mathbf{q}\sim\mathbf{0}$. The result is shown in Fig. 17(b) for $\gamma\equiv M_x/(2m)=M_y/(2m)$.

It is important to note that all the properties of the two-body bound state, including its energy and effective mass, depend on a single parameter $1/(m\lambda a_s)$, which is the ratio of the only two length scales $1/(m\lambda)$ and a_s in the problem. Thus, in the limit of sufficiently large SOC, the bound state becomes universal and is identical to the one obtained at $1/(m\lambda a_s)=0$. This new kind of universal bound state has been referred to as rashbon [21, 25]. The mass of rashbons (i.e., $\gamma\simeq 1.2$ from Fig. 17(b)) is notably heavier than the conventional molecules $2m$ in the BEC limit. This causes a decrease in the condensation temperature of rashbons in such a way that

$$T_{\mathrm{BEC}}=\gamma^{-2/3}T_{\mathrm{BEC}}^{(0)}\simeq 0.193T_F, \tag{59}$$

where $T_{\mathrm{BEC}}^{(0)}\simeq 0.218T_F$ is the BEC temperature of conventional molecules.

In the presence of out-of-plane Zeeman field h, the two-body problem has been discussed in detail in Ref. [24].

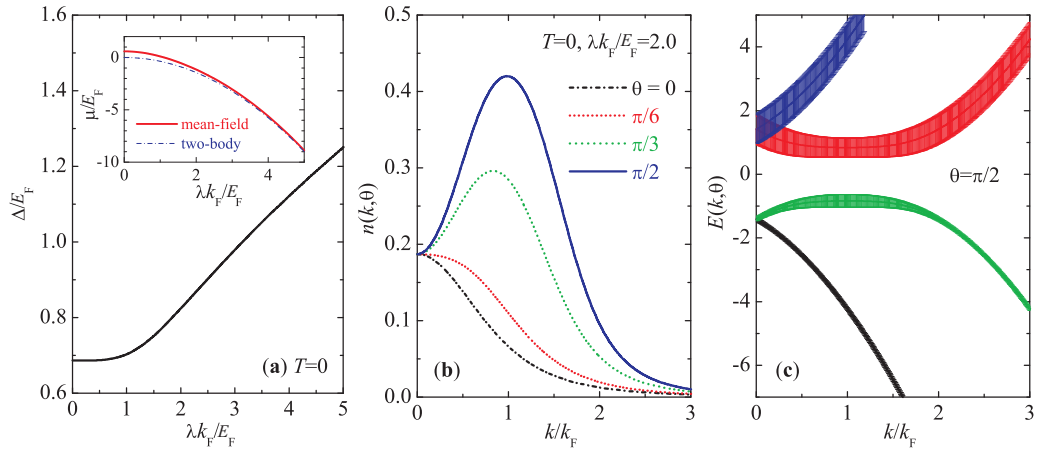

FIG. 18: (a) Mean-field order parameter as a function of the Rashba SOC for a homogeneous unitary Fermi gas at zero temperature. The inset shows the chemical potential and the half of bound state energy, both in units of Fermi energy E_F. (b) Momentum distribution and (c) single-particle spectral function for $\theta = \pi/2$ at $\lambda k_F/E_F = 2$. Here θ is the angle between $\mathbf{k}$ and the z-axis. The width of the curves in (c) represents the weight factor $(1 \pm \gamma_{\mathbf{k},\pm})/4$ for each of the four Bogoliubov excitations. Figure taken from Ref. [22].

3. *Crossover to rashbon BEC and anisotropic superfluidity*

Let us now discuss the crossover to a rashbon BEC. We focus on the unitary limit with $a_s \to \infty$ and increase the 2D Rashba SOC. At the mean-field saddle-point level, the single-particle Green function Eq. (7) takes the form ($h = 0$) [22],

$$G_0^{-1} = \begin{bmatrix} i\omega_m - \xi_{\mathbf{k}} - \lambda(\hat{k}_y\hat{\sigma}_x - \hat{k}_x\hat{\sigma}_y) & i\Delta_0\hat{\sigma}_y \\ -i\Delta_0\hat{\sigma}_y & i\omega_m + \xi_{\mathbf{k}} - \lambda(\hat{k}_y\hat{\sigma}_x + \hat{k}_x\hat{\sigma}_y) \end{bmatrix}. \tag{60}$$

The inversion of the above matrix can be worked out explicitly, leading to two single-particle Bogoliubov dispersions whose degeneracy is lifted by the SOC, $E_{\mathbf{k},\pm} = [(\xi_{\mathbf{k}} \pm \lambda k_\perp)^2 + \Delta_0^2]^{1/2}$, and the normal and anomalous Green functions from which we can immediately obtain the momentum distribution $n(\mathbf{k}) = 1 - \sum_\alpha [1/2 - f(E_{\mathbf{k},\alpha})]\gamma_{\mathbf{k},\alpha}$ and the single-particle spectral function

$$A_{\uparrow\uparrow}(\mathbf{k},\omega) = A_{\downarrow\downarrow}(\mathbf{k},\omega) = \frac{1}{4}\sum_\alpha \left[(1+\gamma_{\mathbf{k},\alpha})\,\delta(\omega - E_{\mathbf{k},\alpha}) + (1-\gamma_{\mathbf{k},\alpha})\,\delta(\omega + E_{\mathbf{k},\alpha})\right], \tag{61}$$

where $\gamma_{\mathbf{k},\pm} = (\xi_{\mathbf{k}} \pm \lambda k_\perp/E_{\mathbf{k},\pm})$. The chemical potential and the order parameter are to be determined by the number and the gap equations, $n = \sum_{\mathbf{k}} n(\mathbf{k})$ and $\Delta_0 = -U_0\Delta_0 \sum_\alpha [1/2 - f(E_{\mathbf{k},\alpha})]/(2E_{\mathbf{k},\alpha})$, respectively. Fig. 18(a) displays the chemical potential μ and the order parameter as functions of the SOC strength. The increase of the SOC strength leads to a deeper bound state. As a consequence, in analogy with the BEC-BCS crossover, the order parameter and the critical transition temperature are greatly enhanced at $\lambda k_F \sim \epsilon_F$. In the large SOC limit, we have $\mu = (\mu_B + E)/2$, where E is the energy of the two-body bound state, and μ_B is positive due to the repulsion between rashbons and decreases with increasing coupling as shown in the inset of Fig. 18(a). By assuming an s-wave repulsion with scattering length a_B between rashbons, where $\mu_B \simeq (n/2)4\pi a_B/M$, we estimate within mean-field that in the unitarity limit, $a_B \simeq 3/(m\lambda)$, comparable to the size of rashbons. Figs. 18(b) and (c) illustrate the momentum distribution and the single-particle spectral function, respectively. These quantities exhibit anisotropic distribution in momentum space due to the SOC and can be readily measured in experiment.

Another interesting feature of the crossover to rashbon BEC is that the pairing field contains both a singlet and a triplet component [97]. For the system under study, it is straightforward to show that the triplet and singlet pairing fields are given by $\langle\psi_{\mathbf{k}\uparrow}\psi_{-\mathbf{k}\uparrow}\rangle = -i\Delta_0 e^{-i\varphi_{\mathbf{k}}} \sum_\alpha \alpha[1/2 - f(E_{\mathbf{k},\alpha})]/(2E_{\mathbf{k},\alpha})$ and $\langle\psi_{\mathbf{k}\uparrow}\psi_{-\mathbf{k}\downarrow}\rangle = \Delta_0 \sum_\alpha [1/2 - f(E_{\mathbf{k},\alpha})]/(2E_{\mathbf{k},\alpha})$, respectively, where $e^{-i\varphi_{\mathbf{k}}} \equiv (k_x - ik_y)/k_\perp$. The magnitude of the pairing fields are shown in Fig. 19(a) and (b). The weight of the triplet component increases and approaches that of the singlet component as the SOC strength increases. In Fig. 19(c) and (d), we plot the zero-momentum dynamic and static spin structure factor, respectively. In the absence of the SOC, both these quantities vanish identically. Hence a nonzero spin structure factor is a direct consequence of triplet pairing [97]. Note that spin structure factor can be measured using the Bragg spectroscopy method as demonstrated in recent experiments [98].

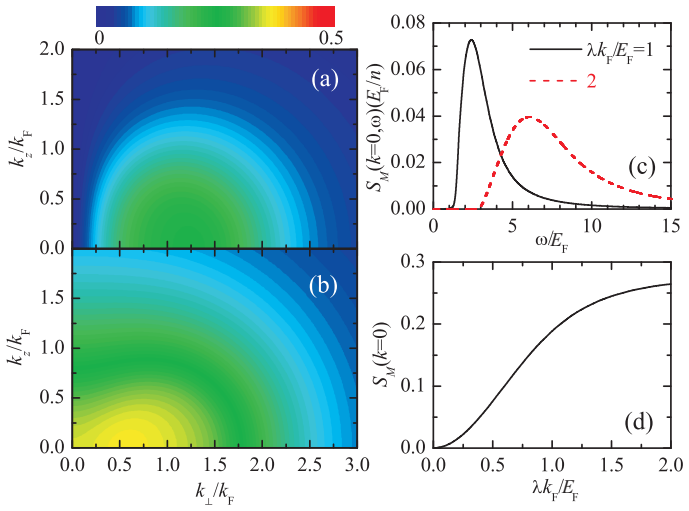

FIG. 19: Linear contour plot for the triple pairing correlation $|\langle\psi_{\mathbf{k}\uparrow}\psi_{-\mathbf{k}\uparrow}\rangle|$ between like spins (a) and the singlet pairing correlation $|\langle\psi_{\mathbf{k}\uparrow}\psi_{-\mathbf{k}\downarrow}\rangle|$ between un-like spins (b) for a homogeneous unitary Fermi gas at zero temperature with $\lambda k_F/E_F = 2$. The zero-momentum dynamic and static spin structure factor are shown in (c) and (d), respectively. Figure taken from Ref. [22].

The condensate fraction and superfluid density of the rashbon system have also been studied [99, 100], and have been found to exhibit unusual behaviors: The condensate fraction is generally enhanced by the SOC due to the increase of the pair binding; while the superfluid density is suppressed because of the nontrivial effective mass of rashbons.

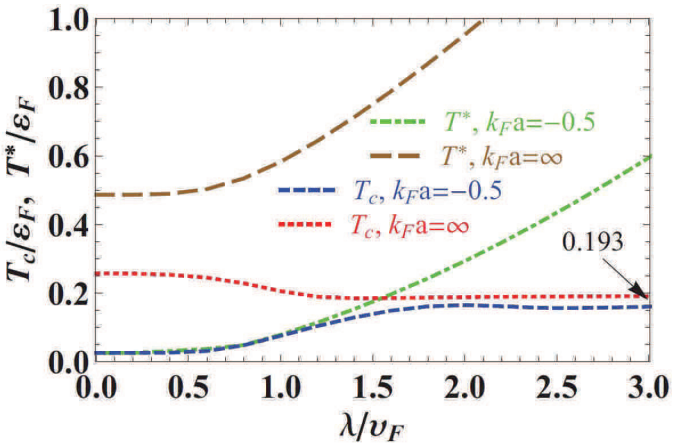

FIG. 20: Critical temperature T_c and the dissociation temperature T^* scaled by the Fermi energy ε_F as a function of the SOC strength λ/v_F for fixed gas parameters $1/(k_F a_s) = -2$ and $1/(k_F a_s) = 0$. Here, we measure the SOC strength in units of Fermi velocity $v_F = k_F/m$. Figure taken from Ref. [28] with modification.

To understand the finite-temperature properties of rashbons, the mean-field approach becomes less reliable. So far, a careful analysis based on the pair-fluctuation theory as outlined in the theoretical framework is yet to be performed. In Fig. 20, we show the superfluid transition temperature as a function of the Rashba SOC strength, predicted by the approximate many-body T-matrix theory - pseudogap theory [28]. At sufficiently large SOC strength, T_c tends to the critical temperature of a rashbon BEC given by Eq. (59) - $T_c \simeq 0.193 T_F$ - regardless of the dimensionless interaction parameter $1/(k_F a_s)$, as we may anticipate. For a more detailed discussion of the crossover from BCS to rashbon BEC, we refer to Ref. [25].

4. 2D Topological superfluidity

Here we consider 2D topological superfluidity with 2D Rashba SOC, in the presence of an out-of-plane Zeeman field h. It is of particular interest, considering the possibility of performing topological quantum computation. This is because each vortex core in a 2D topological superfluid can host a Majorana fermion. Thus, by properly interchanging two vortices and thus braiding Majorana fermions, fault-tolerant quantum information stored non-locally in Majorana fermions may be processed [84, 101]. In the context of ultracold atoms, the use of 2D Rashba SOC to create a 2D topological superfluid was first proposed by Zhang and co-workers [38], and later considered by a number of researchers [41–44, 46, 48–50]. In free space, the criterion to enter topological superfluid phase is given by $h > \sqrt{\mu^2 + \Delta^2}$, above which the system behaves like a 2D weak-coupling p-wave superfluid, as we already discussed in the previous subsection (see, for example, Eq. (48)). Here, we are interested in the nature of 2D topological superfluids for the experimentally relevant situation with the presence of harmonic traps [42].

Theoretically, we solve numerically the BdG equation (29). In the presence of a single vortex at trap center, we take $\Delta_0(\mathbf{r}) = \Delta_0(r)e^{-i\varphi}$ and decouple the BdG equation into different angular momentum channels indexed by an integer m. The quasiparticle wave functions take the form, $[u_{\uparrow\eta}(r)e^{-i\varphi}, u_{\downarrow\eta}(r), v_{\uparrow\eta}(r)e^{i\varphi}, v_{\downarrow\eta}(r)]e^{i(m+1)\varphi}/\sqrt{2\pi}$. We have solved self-consistently the BdG equations using the basis expansion method. For the results presented below, we have taken $N = 400$ and $T = 0$. We have used $E_a = 0.2E_F$ and $\lambda k_F/E_F = 1$, where the binding energy E_a is a useful parameter to characterize the interatomic interaction in 2D. These are typical parameters that can be readily realized in a 2D ^{40}K Fermi gas.

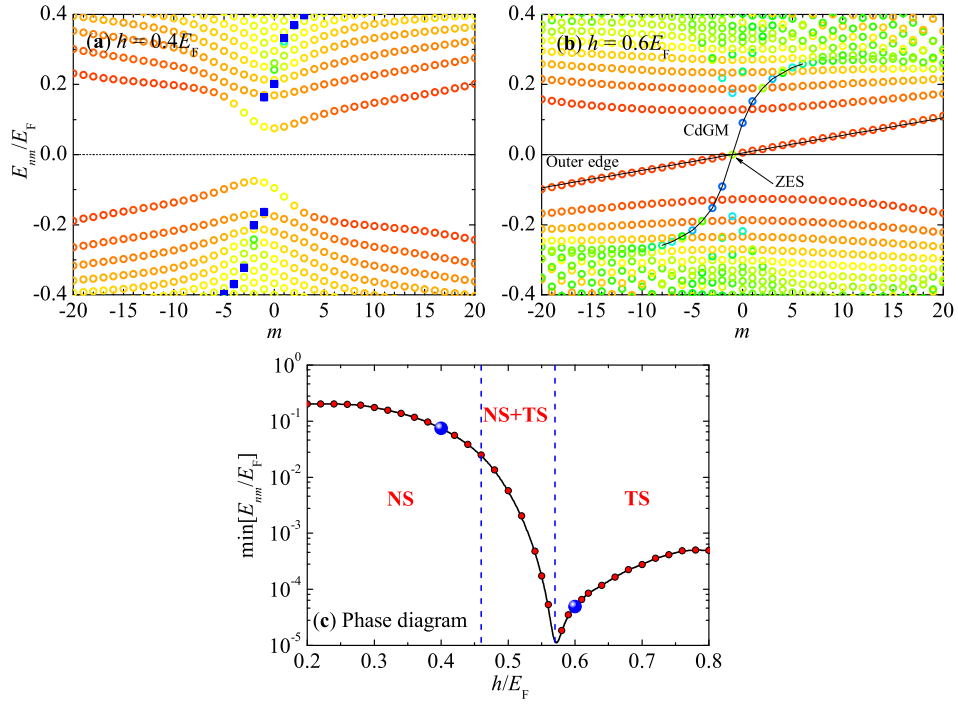

FIG. 21: (a) and (b) Energy spectrum at $h/E_F = 0.4$ and 0.6 (where $E_F = k_F^2/(2M) = \sqrt{N}\omega_\perp$ is the Fermi energy) in the presence of a single vortex. The color of symbols indicates the mean radius $\sqrt{\langle r^2\rangle}/r_F$ (where $r_F = (4N)^{1/4}\sqrt{1/(M\omega_\perp)}$ is the Fermi radius) of the eigenstate, which is defined by $\langle r^2\rangle = \int r^2[|u_\uparrow|^2 + |u_\downarrow|^2 + |v_\uparrow|^2 + |v_\downarrow|^2]d\mathbf{r}$. The color of symbols changes from blue when the excited state is localized at the trap center to red when its mean radius approaches the Thomas-Fermi radius. In (a) and (b), the CdGM states are indicated by blue squares and a solid line, respectively. (c) Phase diagram, along with the lowest eigenenergy of Bogoliubov spectrum. Figure taken from Ref. [42] with modification.

Figs. 21 reports the phase diagram [Fig. 21(c)] along with the quasiparticle energy spectrum of different phases [Figs. 21(a) and 21(b)] in the presence of a single vortex. By increasing the Zeeman field, the system evolves from a non-topological state (NS) to a topological state (TS), through an intermediate mixed phase in which NS and TS coexist. The topological phase transition into TS is well characterized by the low-lying quasiparticle spectrum, which has the particle-hole symmetry $E_{m+1} = -E_{-(m+1)}$. As shown in Fig. 21(a), the spectrum of the NS is gapped. While in the TS, two branches of mid-gap states with small energy spacing appear: One is labeled by "Outer edge" and another "CdGM" which refers to localized states at the vortex core, i.e., the so–called Caroli-de Gennes-Matricon

(CdGM) states [102]. The eigenstates with nearly zero energy at $m = -1$ could be identified as the zero-energy Majorana fermions in the thermodynamic limit.

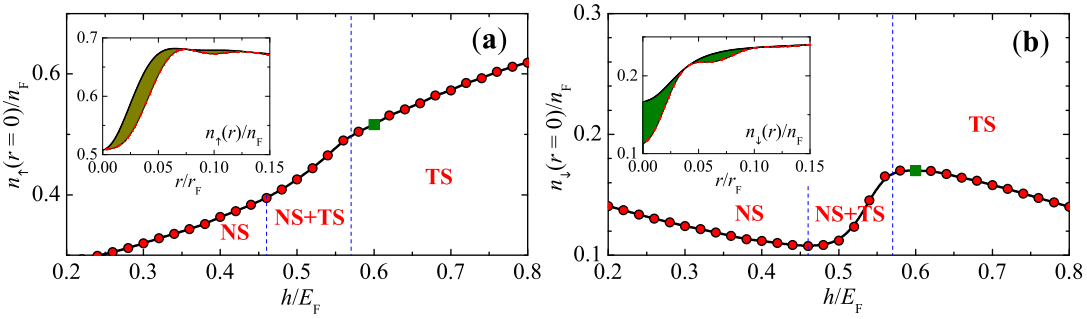

FIG. 22: Zeeman field dependence of spin-up (a) and spin-down (b) densities at the vortex core. The density is normalized by the Thomas-Fermi density $n_F = (\sqrt{N}/\pi)\sqrt{M\omega_\perp}$. The insets show the core density distributions at $h = 0.6E_F$. The red dot-dashed lines show the result by excluding artificially the Majorana vortex core state, whose contribution is shown by the shaded area. Figure taken from Ref. [42] with modification.

In the TS, the occupation of the Majorana vortex-core state affects significantly the atomic density and the local density of states (LDOS) of the Fermi gas near the trap center, which in turn gives a strong experimental signature for observing Majorana fermions. Fig. 22 presents the spin-up and -down densities at the trap center, $n_\uparrow(0)$ and $n_\downarrow(0)$, as a function of the Zeeman field. In general, $n_\uparrow(0)$ and $n_\downarrow(0)$ increases and decreases respectively with increasing field. However, we find a sharp increase of $n_\downarrow(0)$ when the system evolves from the mixed phase to the full TS. Accordingly, a change of slope or kink appears in $n_\uparrow(0)$. The increase of $n_\downarrow(0)$ is associated with the *gradual* formation of the Majorana vortex-core mode, whose occupation contributes notably to atomic density due to the *large* amplitude of its localized wave function. We plot in the inset of Fig. 22(b) $n_\downarrow(0)$ at $h = 0.6E_F$, with or without the contribution of the Majorana mode, which is highlighted by the shaded area. This contribution is apparently absent in the NS. Thus, a sharp increase of $n_\downarrow(0)$, detectable in *in situ* absorption imaging, signals the topological phase transition and the appearance of the Majorana vortex-core mode. This feature persists at typical experimental temperature, i.e., $T = 0.1T_F$.

In the presence of impurity scattering, topological superfluid can also host a universal impurity-induced bound state [50, 51]. That is, regardless of the type of impurities, magnetic or non-magnetic, the impurity will always cause the same bound state within the pairing gap, provided the scattering strength is strong enough. The observation of such a universal impurity-induced bound state will give a clear evidence for the existence of topological superfluids.

III. EXPERIMENTS

We now review the experimental work, focusing on the ones carried out at Shanxi University. The apparatus and cooling scheme in the experiment have been described in previous papers [103–107] and briefly introduced here (see Fig. 1). An atomic mixture sample of ^{87}Rb and ^{40}K atoms in hyperfine state $|F = 2, m_F = 2\rangle$ and $|F = 9/2, m_F = 9/2\rangle$, respectively, are first pre cooled to 1.5 μK by radio-frequency evaporative cooling in a quadrupole-Ioffe configuration (QUIC) trap. The QUIC trap consists of a pair of anti-Helmholtz coils and a third coil in perpendicular orientation. To gain larger optical access, the atoms are first transported from the QUIC trap to the center of the quadrupole coils (glass cell) by lowering the current passing through quadrupole coils and increasing the current in the Ioffe coil, and then are transferred into an crossed optical trap in the horizontal plane, created by two off-resonance laser beams, at a wavelength of 1064 nm. A degenerate Fermi gas of about $N \simeq 2 \times 10^6$ ^{40}K atoms in the $|9/2, 9/2\rangle$ internal state at $T/T_F \simeq 0.3$ is created inside the crossed optical trap. Here T is the temperature and T_F is the Fermi temperature defined by $T_F = E_F/k_B = (6N)^{1/3}\overline{\omega}/k_B$ with a geometric mean trapping frequency $\overline{\omega} \simeq 2\pi \times 130$ Hz. A 780 nm laser pulse of 0.03 ms is used to remove all the ^{87}Rb atoms in the mixture without heating ^{40}K atoms.

To create SOC, a pair of Raman laser beams are extracted from a continuous-wave Ti-sapphire single frequency laser. The two Raman beams are frequency-shifted by two single-pass acousto-optic modulators (AOM) respectively. In this way the relative frequency difference $\Delta\omega$ between the two laser beams is precisely controlled. At the output of the optical fibers, the two Raman beams each has a maximum intensity $I = 130$ mW, counter-propagating along the x-axis with a $1/e^2$ radius of 200 μm and are linearly polarized along the z- and y-axis, respectively, which correspond to π (σ) and σ (π) of the quantization axis $\hat{z}$ ($\hat{y}$). The momentum transferred to atoms during the Raman process is $2k_0 = 2k_r \sin(\theta/2)$, where $k_r = 2\pi/\lambda$ is the single-photon recoil momentum, λ is the wavelength of the Raman

beam, and θ is the intersecting angle of two Raman beams. Here, k_r and $E_r = k_r^2/2m$ are the units of momentum and energy. The optical transition wavelengths of the D1 and D2-line are 770.1 nm and 766.7 nm, respectively. The wavelengths of the Raman lasers are about $772 \sim 773$ nm.

The two internal states involved in SOC are chosen as follows. In the case of noninteracting system, the two states are magnetic sublevels $|\uparrow\rangle = |9/2, 9/2\rangle$ and $|\downarrow\rangle = |9/2, 7/2\rangle$. These two spin states are stable and are weakly interacting with a background s-wave scattering length $a_s = 169a_0$. We use a pair of Helmholtz coils along the y-axis (as shown in Fig. 1) to provide a homogeneous bias magnetic field, which gives a Zeeman shift between the two magnetic sublevels. A Zeeman shift of $\omega_Z = 2\pi \times 10.27$ MHz between these two magnetic sublevels is produced by a homogeneous bias magnetic field of 31 G. When the Raman coupling is at resonance (at $\Delta\omega = 2\pi \times 10.27$ MHz and two-photon Raman detuning $\delta = \Delta\omega - \omega_Z \approx 0$), the detuning between $|9/2, 7/2\rangle$ and other magnetic sublevels like $|9/2, 5/2\rangle$ is about $2\pi \times 170$ kHz, which is one order of magnitude larger than the Fermi energy. Hence all the other states can be safely neglected. In the case of the strongly interacting spin-orbit coupled Fermi gas, two magnetic sublevels $|\downarrow\rangle = |9/2, -9/2\rangle$ and $|\uparrow\rangle = |9/2, -7/2\rangle$ are chosen. To create strong interaction, the bias field is ramped from 204 G to a value near the $B_0 = 202.1$ G Feshbach resonance at a rate of about 0.08 G/ms. We remark that due to a decoupling of the nuclear and electronic spins, the Raman coupling strength decreases with increasing of the bias field [108]. When working at a large bias magnetic field, we have to use a smaller detuning of the Raman beams with respect to the atomic D1 transition in order to increase the Raman coupling strength.

In order to control the magnetic field precisely and reduce the magnetic field noise, the power supply (Delta SM70-45D) has been operated in remote voltage programming mode, whose voltage is set by an analog output of the experiment control system. The current through the coils is controlled by the external regulator relying on a precision current transducer (Danfysik ultastable 867-60I). The current is detected with the precision current transducer, then the regulator compares the measured current value to a set voltage value from the computer. The output error signal from the regulator actively stabilize the current with the PID (proportional-integral-derivative) controller acting on the MOSFET (metal-oxide-semiconductor field-effect transistor). In order to reduce the current noise and decouple the control circuit from the main current, a conventional battery is used to power the circuit.

We use the standard time-of-flight technique to perform our measurement. To this end, the Raman beams, optical dipole trap and the homogeneous bias magnetic field are turned off abruptly at the same time, and a magnetic field gradient along the y-axis provided by the Ioffe coil is turned on. The two spin states are separated along the y-direction, and imaging of atoms along the z-direction after 12 ms expansion gives the momentum distribution for each spin component.

A. The noninteracting spin-orbit coupled Fermi gas

In this section, we review the experiment on non-interacting system.

1. Rabi oscillation

We first study the Rabi oscillation between the two spin states induced by the Raman coupling. All atoms are initially prepared in the $|\uparrow\rangle$ state. The homogeneous bias magnetic field is ramped to a certain value so that $\delta = -4E_r$, that is, the $\mathbf{k} = 0$ component of state $|\uparrow\rangle$ is at resonance with $\mathbf{k} = 2k_r\hat{x}$ state of $|\downarrow\rangle$ component, as shown in Fig. 23(a). Then we apply a Raman pulse to the system, and measure the spin population for different duration time of the Raman pulse. Similar experiment in bosonic system yields an undamped and completely periodic oscillation, which can be well described by a sinusoidal function with frequency Ω [1]. This is because for bosons, macroscopic number of atoms occupy the resonant $\mathbf{k} = 0$ mode, and therefore there is a single Rabi frequency determined by the Raman coupling only. While for fermions, atoms occupy different momentum states. Due to the effect of SOC, the coupling between the two spin states and the resulting energy splitting are momentum dependent, and atoms in different momentum states oscillate with different frequencies. Hence, dephasing naturally occurs and the oscillation will be inevitably damped after several oscillation periods. In our case, the spin-dependent momentum distribution shown in Fig. 23(b) clearly shows the out-of-phase oscillation for different momentum states.

For a non-interacting system, the population of $|\downarrow\rangle$ component is given by

$$n_\downarrow(\mathbf{k} + 2k_r\hat{x}, \mathbf{r}, t) = n_\uparrow(\mathbf{k}, \mathbf{r}, 0)\frac{\sin^2\sqrt{(k_x k_r/m)^2 + \Omega^2/4}\, t}{1 + \left(\frac{2k_x k_r}{\Omega m}\right)^2}, \tag{62}$$

where t is the duration time of Raman pulse, $n_\uparrow(\mathbf{k}, \mathbf{r}, 0)$ is the equilibrium distribution of the initial state in local density approximation. From Eq. (62) one can see that the momentum distribution along the x-axis of the $|\downarrow\rangle$

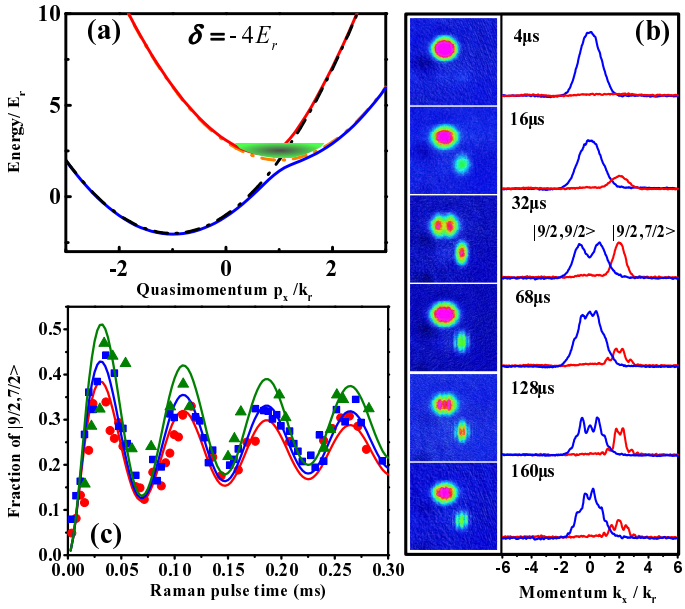

FIG. 23: Raman-induced Rabi oscillation: (a) The energy dispersion with $\delta = -4E_{\rm r}$. The system is initially prepared with all atoms in $|9/2, 9/2\rangle$ state. (b) Time-of-flight image (left) and integrated time-of-flight image (integrated along $\hat{y}$) at different duration time for $|\uparrow\rangle$ (blue) and $|\downarrow\rangle$ (red). The parameters are $k_{\rm F} = 1.35k_{\rm r}$ and $T/T_{\rm F} = 0.35$. (c) The population in $|9/2, 7/2\rangle$ as a function of duration time of Raman pulse. $k_{\rm F} = 1.9k_{\rm r}$ and $T/T_{\rm F} = 0.30$ for red circles, $k_{\rm F} = 1.35k_{\rm r}$ and $T/T_{\rm F} = 0.35$ for blue squares, $k_{\rm F} = 1.1k_{\rm r}$ and $T/T_{\rm F} = 0.29$ for green triangles. The solid lines are theory curves with $\Omega = 1.52E_{\rm r}$. Figure taken from Ref. [11].

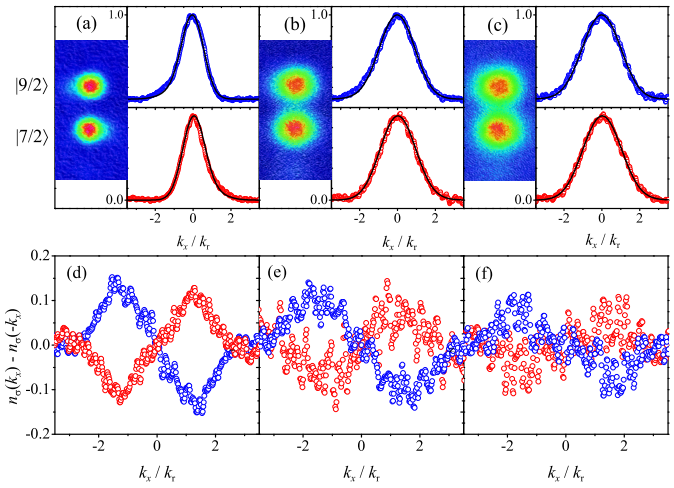

FIG. 24: Momentum distribution asymmetry as a hallmark of SOC: (a-c) time-of-flight measurement of momentum distribution for both $|\uparrow\rangle$ (blue) and $|\downarrow\rangle$ (red). Solid lines are theory curves. (a) $k_{\rm F} = 0.9k_{\rm r}$ and $T/T_{\rm F} = 0.8$ (b) $k_{\rm F} = 1.6k_{\rm r}$ and $T/T_{\rm F} = 0.63$; (c) $k_{\rm F} = 1.8k_{\rm r}$ and $T/T_{\rm F} = 0.57$. (d-f): plot of integrated momentum distribution $n_\sigma(\mathbf{k}) - n_\sigma(-\mathbf{k})$ for the case of (a-c). Figure taken from Ref. [11].

component is always symmetric respect to $2k_{\rm r}$ at any time, which is clearly confirmed by the experimental data as shown in Fig. 23(b). The total population in the $|\downarrow\rangle$ component is given by $N_\downarrow(t) = \int d\mathbf{k}d\mathbf{r}\, n_\downarrow(\mathbf{k}, \mathbf{r}, t)$, and in Fig. 23(c), one can see that there is an excellent agreement between the experiment data and theory, from which we determine $\Omega = 1.52(5)E_{\rm r}$.

2. Momentum distribution

We focus on the case with $\delta = 0$, and study the momentum distribution in the equilibrium state. We first transfer half of ^{40}K atoms from $|\downarrow\rangle$ to $|\uparrow\rangle$ using radio frequency sweep within 100 ms. Then the Raman coupling strength is ramped up adiabatically in 100 ms from zero to its final value and the system is held for another 50 ms before time-of-flight measurement. Since SOC breaks spatial reflection symmetry ($x \to -x$ and $k_x \to -k_x$), the momentum distribution for each spin component will be asymmetric, i.e. $n_\sigma(\mathbf{k}) \neq n_\sigma(-\mathbf{k})$, with $\sigma = \uparrow, \downarrow$. On the other hand, when $\delta = 0$ the system still satisfies $n_\uparrow(\mathbf{k}) = n_\downarrow(-\mathbf{k})$. The asymmetry can be clearly seen in the spin-resolved time-of-flight images and integrated distributions displayed in Fig. 24(a) and (b), where the fermion density is relatively low. While it becomes less significant when the fermion density becomes higher, as shown in Fig. 24(c), because the strength of the SOC is relatively weaker compared to the Fermi energy. Although the presence of the Raman lasers cause additional heating to the cloud, we find that the temperature is within the range of $0.5 - 0.8T_\mathrm{F}$, which is still below degenerate temperature. In Fig. 24(d-f), we also show $n_\sigma(k_x) - n_\sigma(-k_x)$ to reveal the momentum distribution asymmetry more clearly.

3. Lifshitz transition

With SOC, the single particle spectra of Eq. (39) are dramatically changed from two parabolic dispersions into two helicity branches as shown in Fig. 25(b). Here, two different branches are eigenstates of "helicity" $\hat{s}$ and the "helicity" operator describes whether spin $\boldsymbol{\sigma}_\mathbf{p}$ is parallel or anti-parallel to the "effective Zeeman field" $\mathbf{h} = (-\Omega, 0, k_\mathrm{r}p_x/m + \delta)$ at each momentum, i.e. $\hat{s} = \boldsymbol{\sigma}_\mathbf{p} \cdot \mathbf{h}/|\boldsymbol{\sigma}_\mathbf{p} \cdot \mathbf{h}|$. $s = 1$ for the upper branch and $s = -1$ for the lower branch. The topology of Fermi surface exhibits two transitions as the atomic density varies. At sufficient low density, it contains two disjointed Fermi surfaces with $s = -1$, and they gradually merge into a single Fermi surface as the density increases to n_{c1}. Finally a new small Fermi surface appears at the center of large Fermi surface when density further increases and fermions begin to occupy $s = 1$ helicity branch at n_{c2}. A theoretical ground state phase diagram for the uniform system is shown in Fig. 25(a), and an illustration of the Fermi surfaces at different density are shown in Fig. 25(b). Across the phase boundaries, the system experiences Lifshitz transitions as density increases [109], which is a unique property in a Fermi gas due to Pauli principle.

We fix the Raman coupling and vary the atomic density at the center of the trap, as indicated by the red arrow in Fig. 25(a). In Fig. 25(c1-c5), we plot the quasi-momentum distribution in the helicity bases for different atomic density. At the lowest density, the $s = 1$ helicity branch is nearly unoccupied, which is consistent with that the Fermi surface is below $s = 1$ helicity branch. The quasi-momentum distribution of the $s = -1$ helicity branch exhibits clearly a double-peak structure, which reveals that the system is close to the boundary of having two disjointed Fermi surfaces at $s = -1$ helicity branch. As density increases, the double-peak feature gradually disappears, indicating the Fermi surface of $s = -1$ helicity branch finally becomes a single elongated one, as the top one in Fig. 25(b). Here we define a quality of visibility $v = (n_\mathrm{A} - n_\mathrm{B})/(n_\mathrm{A} + n_\mathrm{B})$, where n_A is the density of $s = -1$ branch at the peak and n_B is the density at the dip between two peaks. Theoretically one expects v approaches unity at low density regime and approaches zero at high density regime. In Fig. 25(d) we show that our data decreases as density increases and agrees very well with a theoretical curve with a fixed temperature of $T/T_\mathrm{F} = 0.65$. Moreover, across the phase boundary between SFS and DFS-1, one expects a significant increase of population on $s = 1$ helicity branch. In Fig. 25(e), the fraction of atom number population at $s = 1$ helicity branch is plotted as a function of Fermi momentum k_F, which grows near the critical point predicted in zero-temperature phase diagram. The blue solid line is a theoretical calculation for N_+/N with $T/T_\mathrm{F} = 0.65$, and the small deviation between the data and this line is due to the temperature variation between different measurements. Because the temperature is too high, the transition is smeared out. For both v and N_+/N we observe only a smooth decreasing or growth across the regime where it is supposed to have a sharp transition, however, the agreement with theory suggests that with better cooling a sharper transition should be observable.

4. Momentum-resolved rf spectrum

The effect of SOC is further studied with momentum resolved rf spectroscopy [71], which maps out the single-particle dispersion relation. A Gaussian shaped pulse of rf field is applied for 200 μs to transfer atoms from $|9/2, 7/2\rangle$ ($|\downarrow\rangle$) state to the final state $|9/2, 5/2\rangle$, as shown in Fig. 26(a), and then the spin population at $|9/2, 5/2\rangle$ is measured with time-of-flight at different rf frequencies. In Fig. 26(b) we plot an example of the final state population as a function of momentum p_x and the frequency of rf field ν_RF, from which one can clearly see the back-bending feature and the gap opening at the Dirac point. Both are clear evidences of SOC.

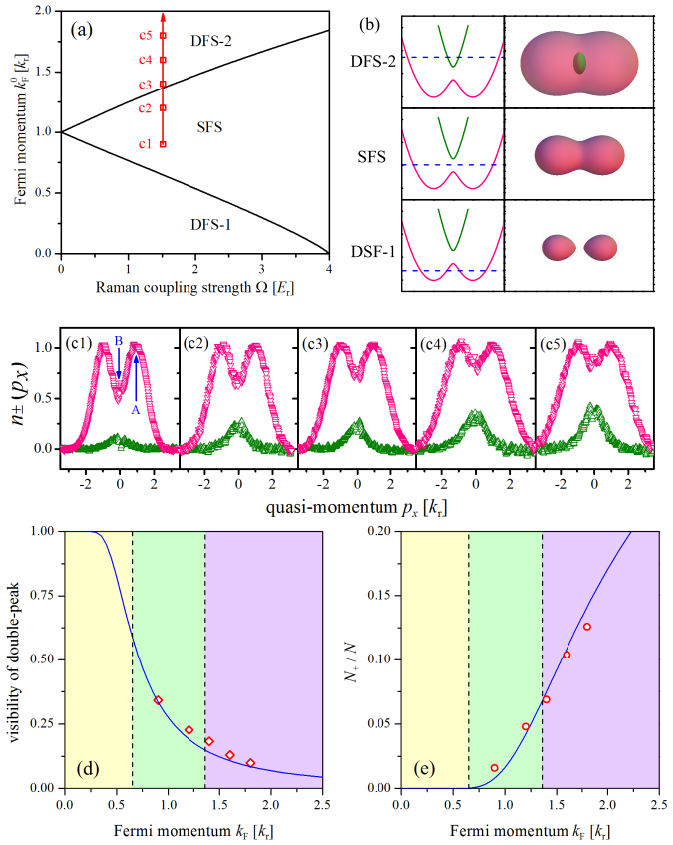

FIG. 25: Topological change of Fermi surface and Lifshitz transition: (a) Theoretical phase diagram at $T = 0$. $k_{\rm F}^0 = (3\pi^2 n)^{1/3}$. "SFS" means single Fermi surface. "DFS" means double Fermi surface. (b) Illustration of different topology of Fermi surfaces. The single particle energy dispersion is drawn for small Ω. Dashed blue line is the chemical potential. (c) Quasi-momentum distribution in the helicity bases. Red and green points are distributions for $s = -1$ and $s = 1$ helicity branches, respectively. $k_{\rm F} = 0.9k_{\rm r}$, $T/T_{\rm F} = 0.80$ for (c1); $k_{\rm F} = 1.2k_{\rm r}$, $T/T_{\rm F} = 0.69$ for (c2); $k_{\rm F} = 1.4k_{\rm r}$, $T/T_{\rm F} = 0.61$ for (c3); $k_{\rm F} = 1.6k_{\rm r}$, $T/T_{\rm F} = 0.63$ for (c4); $k_{\rm F} = 1.8k_{\rm r}$, $T/T_{\rm F} = 0.57$ for (c5). All these points are marked on phase diagram in (a). (d) Visibility $v = (n_{\rm A} - n_{\rm B})/(n_{\rm A} + n_{\rm B})$ decreases as $k_{\rm F}/k_{\rm r}$ increases (A and B points are marked in (c1)). (e) Atom number population in $s = 1$ helicity branch N_+/N increases as $k_{\rm F}/k_{\rm r}$ increases increases. In both (d) and (e), the blue solid line is a theoretical curve with $T/T_{\rm F} = 0.65$, and the background color indicates three different phases in the phase diagram. Figure taken from Ref. [11].

For an occupied state, the initial state dispersion $\epsilon_i(\mathbf{k})$ can be mapped out by

$$\epsilon_i(\mathbf{k}) = \nu_{RF} - E_Z + \epsilon_f(\mathbf{k}). \tag{63}$$

where $\epsilon_f(\mathbf{k}) = \mathbf{k}^2/2m$ is the dispersion of the final $|9/2, 5/2\rangle$ state, and E_Z is the energy difference between $|9/2, 7/2\rangle$ and $|9/2, 5/2\rangle$ state. Here, the momentum of the rf photon is neglected, thus the rf pulse does not impart momentum to the atom in the final state. In Fig. 26(c) we show three measurements corresponding to (c1), (c3) and (c5) in Fig. 25. For (c1), clearly only $s = -1$ branch is populated. For (c3), the population is slightly above the $s = 1$ helicity branch. And for (c5), there are already significant population at $s = 1$ helicity branch. In (c5) one can also identify the chiral nature of two helicity branches: For $s = -1$ branch, most left-moving states are dominated by $|\downarrow\rangle$ state; while for $s = 1$ branch, right-moving states are mostly dominated by $|\downarrow\rangle$ states.

The theoretical simulation of momentum-resolved rf spectroscopy has been performed and discussed in Sec. II B 1 (see, in particular, Fig. 3). We note that, the definition of momentum and rf frequency is different. These are related by, $k_x = -p_x - k_r$ and $\omega = -\nu_{RF}$.

The single-particle spectrum is also measured using the technique of spin injection spectroscopy in a spin-orbit coupled Fermi gas of ^{6}Li by the MIT group [12]. In that work, the following four lowest hyperfine states are chosen $|3/2, -1/2\rangle$, $|3/2, -3/2\rangle$, $|1/2, -1/2\rangle$, $|1/2, 1/2\rangle$, which are labelled as $|\uparrow\rangle_i$, $|\uparrow\rangle_f$, $|\downarrow\rangle_f$, $|\downarrow\rangle_i$. The Raman process couples $|\uparrow\rangle_f$ to $|\downarrow\rangle_f$ to induce SOC between these two states. For momentum-resolved rf spectroscopy, the state $|\downarrow\rangle_i$ is coupled via rf field to the state $|\downarrow\rangle_f$, as this connects the first and second lowest hyperfine states. Similarly, an atom in state

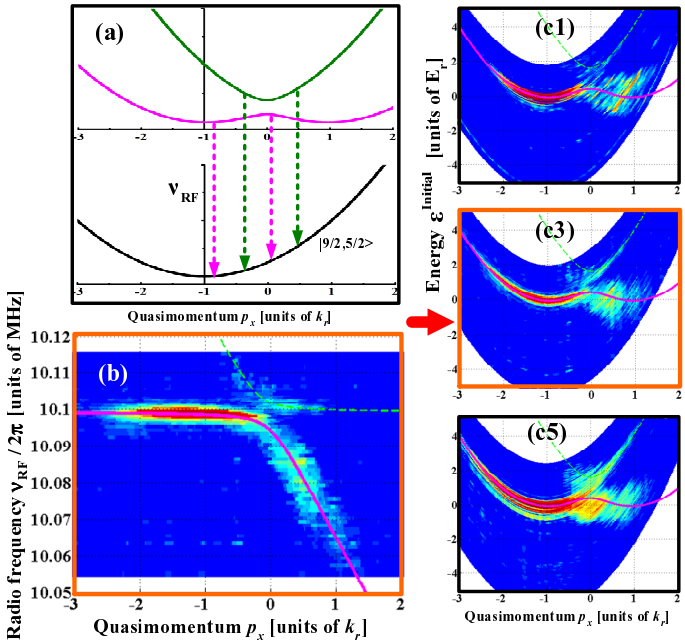

FIG. 26: Momentum-resolved rf spectroscopy of a spin-orbit coupled Fermi gas: (a) Schematic of momentum-resolved rf spectroscopy of SO coupled Fermi gases. Green and pink solid lines are two helicity branches in which the eigenstates are all superposition of $|9/2, 9/2\rangle$ and $|9/2, 7/2\rangle$. Thus both can undergo rf transition from $|9/2, 7/2\rangle$ to $|9/2, 5/2\rangle$, as indicated by dashed lines. (b) Intensity map of the atoms in $|9/2, 5/2\rangle$ state as a function of (ν_{RF}, k_x) plane. (c) Single particle dispersion and atom population measured for (c1), (c3) and (c5) in Fig. 25. Figure taken from Ref. [11].

$|\uparrow\rangle_i$ is coupled to $|\uparrow\rangle_f$. Since the dispersion for initial states $|\uparrow\rangle_i$ and $|\downarrow\rangle_i$ ($\epsilon_i(\mathbf{k}) = \mathbf{k}^2/2m$) are known, the spectra of the final states, which is subject to the SOC, are obtained.

The dispersion investigated above is the simplest case for a spin-orbit coupled system. An even richer band structure involving multiple spinful bands separated by fully insulating gaps can arise in the presence of a periodic lattice potential. This has been realized for Bose-Einstein condensates by adding rf coupling between the Raman-coupled states $|\uparrow\rangle_f$ and $|\downarrow\rangle_f$ [110]. Using a similar method, a spinful lattice for ultracold fermions is created, and one can use spin-injection spectroscopy to probe the resulting spinful band structure [12], see, for example, Fig. 4.

B. The strongly interacting spin-orbit coupled Fermi gas

We now consider the Femi gas where interaction cannot be neglected. In particular, we focus on the effect of SOC on fermionic pairing.

1. *Integrated radio-frequency spectrum*

To create a strongly interacting Fermi gas with spin-orbit coupling, first, the bias magnetic field is tuned from high magnetic field above Feshbach resonance to a final value B (which is varied) below Feshbach resonance. Thus, Feshbach molecules are created in this process. Then, we ramp up adiabatically the Raman coupling strength in 15 ms from zero to its final value $\Omega = 1.5E_r$ with Raman detuning $\delta = 0$. The temperature of the Fermi cloud after switching on the Raman beams is at about $0.6T_F$ [11]. The Fermi energy is $E_F \simeq 2.5E_r$ and the corresponding Fermi wavevector is $k_F \simeq 1.6k_r$. To characterize the strongly-interacting spin-orbit coupled Fermi system, we apply a Gaussian shaped pulse of rf field with a duration time about 400 μs and frequency ω to transfer the spin-up fermions to an un-occupied third hyperfine state $|3\rangle = |F = 9/2, m_F = -5/2\rangle$.

In Fig. 27(b), we show that the integrated rf-spectrum of an interacting Fermi gas below the Feshbach resonance, with or without spin-orbit coupling. Here, we carefully choose the one photon detuning of the Raman lasers to avoid shifting Feshbach resonance by the Raman laser on the bound-to-bound transition between the ground Feshbach molecular state and the electronically excited molecular state. We also make sure that the single-photon process does

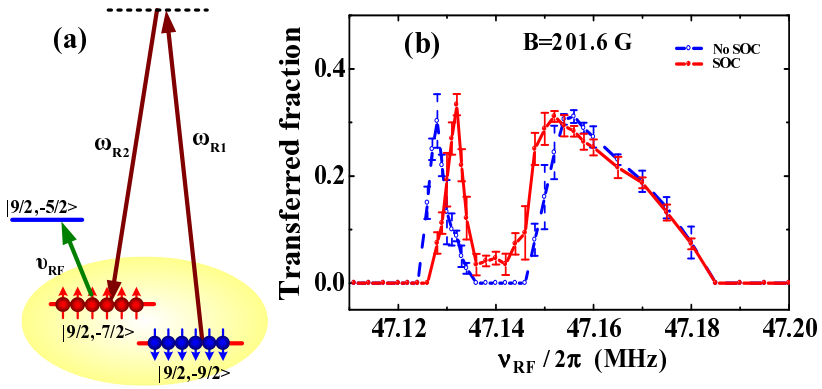

FIG. 27: (a) Energy level of a strongly-interacting Fermi gas of ^{40}K atoms with SOC. (b) The integrated rf-spectroscopy below the Feshbach resonance (at $B = 201.6$ G and $a_s \simeq 2215.6a_0$, where a_0 is the Bohr radius), in the presence (solid circles) and absence (empty circles) of the spin-orbit coupling. The Raman detuning is $\delta = 0$. The dimensionless interaction parameter $1/(k_F a_s) \simeq 0.66$. The fraction is defined as $N_{-5/2}/(N_{-5/2} + N_{-7/2})$, where $N_{-5/2}$ and $N_{-7/2}$ are obtained from the TOF absorption image. Figure taken from Ref. [13].

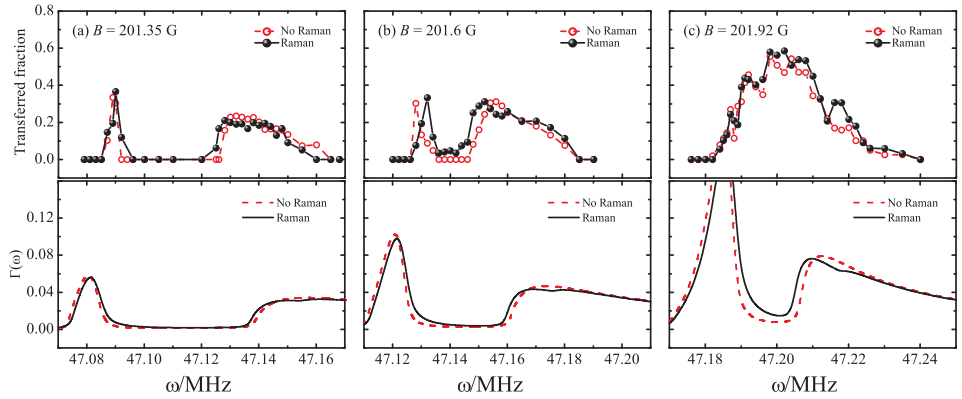

FIG. 28: The integrated rf-spectrum for a spin-orbit coupled Fermi gas. The red solid circles (red lines) and dark empty circles show respectively the experimental data in the presence and absence of spin-orbit coupling with Raman detuning $\delta = 0$. The upper panel represents experimental data and the lower panel represents the theoretical calculation. The dimensionless interaction parameter $1/(k_F a_s)$ in (a), (b), and (c) are 0.89, 0.66, and 0.32, respectively. Figure taken from Ref. [13].

not affect the rf spectrum. The narrow and broad peaks in the spectrum should be interpreted respectively as the rf-response from free atoms and fermionic pairs. With spin-orbit coupling, we find a systematic blue shift in the atomic response and a red shift in the pair response. The latter is an unambiguous indication that the properties of fermionic pairs are strongly affected by spin-orbit coupling [13]. The red shift of the response from the pairs may be understood from the binding energy of pairs in the two-body limit. As mentioned below Eq. (39), the Raman coupling may be regarded as an effective Zeeman field. The stronger the effective Zeeman field, the smaller the binding energy of the two-particle bound states [24, 26].

In Fig. 28, we compare the experimentally measured rf-spectrum with the many-body T-matrix prediction, which is obtained within the pseudogap approximation [13] (see the discussion in Sec. II A 3 and II A 5). In the calculation, at a qualitative level, we do not consider the trap effect and take the relevant experimental parameters at the trap center. Otherwise, there are no adjustable free parameters used in the theoretical calculations. As shown in Fig. 28, we find a qualitative agreement between theory and experiment, both of which show the red shift of the response from fermionic pairs. Note that, near Feshbach resonances our many-body pseudogap theory is only qualitatively reliable. It cannot explain well the separation of atomic and pair peaks in the observed integrated rf-spectrum. More seriously, it fails to take into account properly the strong interactions between atoms and pairs.

2. Coherent formation of Feshbach molecules by spin-orbit coupling

In a recent experiment, we studied the formation of Feshbach molecules from an initially spin-polarized Fermi gas [15]. For simplicity, let us consider two atoms both prepared in the $|\downarrow\rangle$ state. We label this state as $|\downarrow\rangle_1|\downarrow\rangle_2$, which is obviously a spin-symmetric state. Under the s-wave interaction, the Feshbach molecule is spin-antisymmetric singlet state. Hence to form Feshbach molecule from this initial state, a spin-antisymmetric coupling is required. To this end, we apply two Raman laser beams that effectively couples the hyperfine states $|\uparrow\rangle$ and $|\downarrow\rangle$. The effective Hamiltonian arising from the Raman beams can be written as $H_R = H_R^{(1)} + H_R^{(2)}$ with

$$H_R^{(j)} = -\frac{\delta}{2}\sigma_z^{(j)} + \frac{\Omega}{2}e^{2ik_0x_j}\sigma_+^{(j)} + \frac{\Omega}{2}e^{-2ik_0x_j}\sigma_-^{(j)}, \tag{64}$$

for $j = 1, 2$. Here we have $\sigma_z^{(j)} = (|\uparrow\rangle_j\langle\uparrow| - |\uparrow\rangle_j\langle\uparrow|)/2$, $\sigma_+^{(j)} = |\uparrow\rangle_j\langle\downarrow|$, and $\sigma_-^{(j)} = \sigma_+^{(j)\dagger}$. In Eq. (64), Ω is the Raman coupling intensity, x_j is the position of the j-th atom in the x-direction, and $k_0 = k_r \sin(\theta/2)$, with k_r the single-photon recoil momentum and θ the angle between the two Raman beams. It is apparent that H_R can be written as $H_R = H_R^{(+)} + H_R^{(-)}$ with

$$H_R^{(\pm)} = \frac{\Omega}{4}\left(e^{i2k_0x_1} \pm e^{i2k_0x_2}\right)\left(\sigma_+^{(1)} \pm \sigma_+^{(2)}\right) + h.c.. \tag{65}$$

Obviously, $H_R^{(-)}$ and $H_R^{(+)}$ are *anti-symmetric* and *symmetric* under the exchange of the hyperfine state of the two atoms, respectively. Therefore, only $H_R^{(-)}$ can create spin-antisymmetric state out of the initially polarized state $|\downarrow\rangle_1|\downarrow\rangle_2$, and as a consequence make the formation of Feshbach molecule possible. When the two Raman beams propagate along the same direction, i.e., $\theta = 0$, we have $k_0 = 0$ and thus $H_R^{(-)} = 0$. Then the Feshbach molecule cannot be produced from the polarized atoms. In contrast, when the angle θ between the two Raman beams is non-zero, we have $H_R^{(-)} \neq 0$ and Feshbach molecule can thus be created.

This picture is exactly confirmed by our data. Our experiment is performed with the spin polarized ^{40}K gas in $|F, m_F\rangle = |9/2, -9/2\rangle$ state, at 201.4 G, below the Feshbach resonance located at 202.1 G, which corresponds to a binding energy of $E_b = 2\pi \times 30$ kHz (corresponding to $3.59E_r$) for the Feshbach molecules and $1/(k_F a_s) \approx 0.92$ for our typical density. After applying the Raman lasers for certain duration time, we turn off the Raman lasers and measure the population of Feshbach molecule and atoms in $|9/2, -7/2\rangle$ state with an rf pulse. This rf field drives a transition from $|9/2, -7/2\rangle$ to $|9/2, -5/2\rangle$. For a mixture of $|9/2, -7/2\rangle$ and Feshbach molecules, as a function of rf frequency ν_{RF}, we find two peaks in the population of $|9/2, -5/2\rangle$, as shown in Fig. 29(b). The first peak (blue curve) is attributed to free atom-atom transition and the second peak (red curve) is attributed to molecule-atom transition. Thus, in the following, we set $\nu_{RF}/2\pi$ to 47.14 MHz to measure Feshbach molecules.

When the two-photon Raman detuning δ is set to $\delta = -E_b = -3.59E_r$, as shown in Fig. 29(a), we measure the population of Feshbach molecule as a function of duration time for three different angles, $\theta = 180°$, $\theta = 90°$, and $\theta = 0°$, as shown in Fig. 29(c), (d) and (e). We find for $\theta = 180°$, Feshbach molecules are created by Raman process and the coherent Rabi oscillation between atom-molecule can be seen clearly. For $\theta = 90°$, production of Feshbach molecules is reduced a little bit and the atom-molecule Rabi oscillation becomes invisible. For $\theta = 0°$, no Feshbach molecule is created even up to 40 ms, which means the transition between Feshbach molecules and a fully polarized state is prohibited if Raman process imparts no momentum transfer, i.e., no SOC.

In a related work, the NIST group recently carried out an experiment in which they swept a magnetic field on the BEC side of the Feshbach resonance [14]. It is shown that the number of remaining atoms exhibits a dip as a function of the magnetic field strength. This dip represents the loss of atom due to the formation of the Feshbach molecules. The position of the dip moves towards the lower field (to the BEC limit) as the Raman detuning δ is increased. The phenomenon can also be explained by the fact that the effective Zeeman field (in this case, the detuning δ) disfavors the formation of bound molecules. Hence at larger δ, a larger a_s^{-1} (i.e., stronger attraction between unlike spins) is required to form molecules [26]. This is in full agreement with the theoretical discussion concerning the two-body physics for the equal-weight Rashba-Dresselhaus SOC presented in Sec. II B 2.

IV. CONCLUSION

In this chapter, we described the properties of a spin-orbit coupled Fermi gas. Recent progress, both theoretical and experimental, were reviewed. As we have shown, spin-orbit coupled Fermi gases possess a variety of intriguing properties. The diverse configuration of the synthetic Gauge field and the extraordinary controllability of atomic systems provide new opportunities to explore quantum many-body systems and quantum topological matter. We

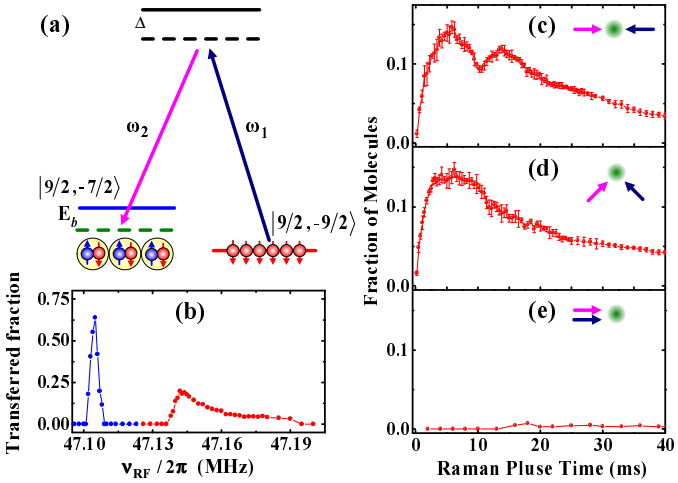

FIG. 29: Energy level diagram and spin-orbit coupling induced Feshbach molecules. **(a)** Schematic diagram of the energy levels. A pair of Raman lasers couples spin polarized state $|9/2, -9/2\rangle$ to Feshbach molecules in Fermi gases ^{40}K. **(b)** Radio-frequency spectrum $|9/2, -7/2\rangle$ to $|9/2, -5/2\rangle$ transition applied to a mixture of Feshbach molecules and scattering atoms in $|9/2, -7/2\rangle$. **(c-e)** The population of Feshbach molecules detected by the rf pulse as a function of duration time of the Raman pulse. The angle of two Raman beams is $\theta = 180^\circ$ (c), $\theta = 90^\circ$ (d) and $\theta = 0^\circ$ (e). The Raman coupling strength is $\Omega = 1.3E_r$ and the two-photon Raman detuning is $\delta = -E_b = -3.59E_r$. Figure taken from Ref. [15].

note that this article by no means is a comprehensive review. For example, we only focused on a continuum system and neglected many interesting theoretical works on lattice systems.

So far only one particular scheme (equal-weight Rashba-Dresselhaus) of SOC has been realized in the experiment, which is based on the Raman transition between two hyperfine ground states of the atom. One drawback of the laser-based SOC generating scheme is that the application of the laser fields inevitably induce additional heating. For certain atoms, this heating may be severe enough to prevent the system from becoming quantum degenerate. Furthermore, many interesting physics requires a strong interaction strength which is induced by applying a fairly strong magnetic field via the Feshbach resonance. Due to a decoupling of the nuclear and electronic spins in large magnetic fields, Raman coupling efficiency quickly reduces with increasing of the magnetic field [108]. This poses another severe experimental challenge. Due to these reasons, no superfluid spin-orbit coupled Fermi gas has been realized yet. As a result, many interesting theoretical proposals (e.g., topological superfluids, Majorna fermion, etc.) are still waiting to be experimentally realized. Nevertheless, we want to remark that despite the relatively high temperature of the experimental system, the effects of SOC have been clearly revealed in single-particle properties as well as the two- and many-body properties on the BEC side of the resonance, as such properties are not easily washed out by finite temperature effects. Very recently, a scheme to synthesize a general SOC is proposed, which is based on purely magnetic field pulses and involves no laser fields [111, 112]. Whether this scheme will overcome the problems mentioned above remains to be seen.

Acknowledgments

We are deeply appreciative for discussions with Congjun Wu, Wei Yi, Hui Zhai, Chuanwei Zhang, and many others; as well as the students and postdocs in our groups: Lin Dong, Lei Jiang, Shi-Guo Peng, Pengjun Wang, and Zhengkun Fu. JZ is supported by NFRP-China (Grant No. 2011CB921601), NSFC Project for Excellent Research Team (Grant No. 61121064), NSFC (Grant No. 11234008), Doctoral Program Foundation of Ministry of Education China (Grant No. 20111401130001). XJL and HH are supported by the ARC DP0984637 and DP0984522. HP is supported by the NSF, the DARPA OLE program and the Welch Foundation (Grant No. C-1669).

[1] Y.-J. Lin, R. L. Compton, A. R. Perry, W. D. Phillips, J. V. Porto, and I. B. Spielman, Phys. Rev. Lett. **102**, 130401 (2009).
[2] Y.-J. Lin, R. L. Compton, K. Jiménez-García, J. V. Porto, and I. B. Spielman, Nature (London) **462**, 628 (2009).

[3] Y-J. Lin, R. L. Compton, K. Jiménez-García, W. D. Phillips, J. V. Porto, and I. B. Spielman, Nature Phys. **7**, 531 (2011).
[4] The quantum version of Maxwell's theory is described by quantum electrodynamics, which is a dynamic gauge theory in the sense that the gauge symmetries generate dynamics by giving rise to interaction couplings between particles mediated by photons. The artificial gauge fields for cold atoms, by contrast, are static, i.e., not dynamically coupled to the atomic fields.
[5] I. B. Spielman, Chapter 5 in *Annual Review of Cold Atoms and Molecules*, Vol. 1 (World Scientific, 2012), edited by K. Madison, Y. Wang, A. M. Rey, and K. Bongs.
[6] Y.-J. Lin, K. Jiménez-García, and I. B. Spielman, Nature (London) **471**, 83 (2011).
[7] Z. Fu, P. Wang, S. Chai, L. Huang, and J. Zhang, Phys. Rev. A **84**, 043609 (2011).
[8] J.-Y. Zhang, S.-C. Ji, Z. Chen, L. Zhang, Z.-D. Du, B. Yan, G.-S. Pan, B. Zhao, Y.-J. Deng, H. Zhai, S. Chen, and J.-W. Pan, Phys. Rev. Lett. **109**, 115301 (2012).
[9] C. Qu, C. Hamner, M. Gong, C. Zhang, and P. Engels, arXiv:1301.0658.
[10] J.-Y. Zhang, S.-C. Ji, L. Zhang, Z.-D. Du, W. Zheng, Y.-J. Deng, H. Zhai, S. Chen, and J.-W. Pan, arXiv:1305.7054.
[11] P. Wang, Z. Yu, Z. Fu, J. Miao, L. Huang, S. Chai, H. Zhai, and J. Zhang, Phys. Rev. Lett. **109**, 095301 (2012).
[12] L. W. Cheuk, A. T. Sommer, Z. Hadzibabic, T. Yefsah, W. S. Bakr, and M. W. Zwierlein, Phys. Rev. Lett. **109**, 095302 (2012).
[13] Z. Fu, L. Huang, Z. Meng, P. Wang, X.-J. Liu, H. Pu, H. Hu, and J. Zhang, Phys. Rev. A **87**, 053619 (2013).
[14] R. A. Williams, M. C. Beeler, L. J. LeBlanc, K. Jimenez-Garcia, and I. B. Spielman, Phys. Rev. Lett. **111**, 095301 (2013).
[15] Z. Fu, L. Huang, Z. Meng, P. Wang, L. Zhang, S. Zhang, H. Zhai, P. Zhang, and J. Zhang, arXiv:1306.4568.
[16] M. Z. Hasan, and C. L. Kane, Rev. Mod. Phys. **82**, 3045 (2010).
[17] D. Xiao, M.-C. Chang, and Q. Niu, Rev. Mod. Phys. **82**, 1959 (2010).
[18] C. Chin, R. Grimm, P. Julienne, and E. Tiesinga, Rev. Mod. Phys. **82**, 1225 (2010).
[19] S. Giorgini, L. Pitaevskii, and S. Stringari, Rev. Mod. Phys. **80**, 1215 (2008).
[20] J. P. Vyasanakere, S. Zhang, and V. B. Shenoy, Phys. Rev. B **84**, 014512 (2011).
[21] J. P. Vyasanakere, and V. B. Shenoy, Phys. Rev. B **83**, 094515 (2011).
[22] H. Hu, L. Jiang, X. -J. Liu and H. Pu, Phys. Rev. Lett. **107**, 195304 (2011).
[23] Z.-Q. Yu, and H. Zhai, Phys. Rev. Lett. **107**, 195305 (2011).
[24] L. Jiang, X.-J. Liu, H. Hu, and H. Pu, Phys. Rev. A **84**, 063618 (2011).
[25] J. P. Vyasanakere, and V. B. Shenoy, New J. Phys. 14, 043041 (2012).
[26] L. Dong, L. Jiang, H. Hu, and H. Pu, Phys. Rev. A **87**, 043616 (2013).
[27] L. Han and C. A. R. Sá de Melo, Phys. Rev. A **85**, 011606 (2012).
[28] L. He, X.-G. Huang, H. Hu, and X.-J. Liu, Phys. Rev. A **87**, 053616 (2013).
[29] Z. Zheng, M. Gong, X. Zou, C. Zhang, and G.-C. Guo, Phys. Rev. A 87, 031602(R) (2013).
[30] V. B. Shenoy, Phys. Rev. A **88**, 033609 (2013).
[31] Z. Zheng, M. Gong, Y. Zhang, X. Zou, C. Zhang, and G.-C. Guo, arXiv:1212.6826.
[32] F. Wu, G.-C. Guo, W. Zhang, and W. Yi, Phys. Rev. Lett. **110**, 110401 (2013).
[33] X.-J. Liu and H. Hu, Phys. Rev. A **87**, 051608(R) (2013).
[34] L. Dong, L. Jiang, and H. Pu, New J. Phys. **15**, 075014 (2013).
[35] H. Hu and X.-J. Liu, arXiv:1304.0387.
[36] X.-F. Zhou, G.-C. Guo, W. Zhang, and W. Yi, Phys. Rev. A **87**, 063606 (2013).
[37] M. Iskin, Phys. Rev. A **88**, 013631 (2013).
[38] C. Zhang, S. Tewari, R. Lutchyn, and S. Das Sarma, Phys. Rev. Lett. **101**, 160401 (2008).
[39] M. Gong, S. Tewari, and C. Zhang, Phys. Rev. Lett. **107**, 195303 (2011).
[40] L. Jiang, T. Kitagawa, J. Alicea, A. R. Akhmerov, D. Pekker, G. Refael, J. I. Cirac, E. Demler, M. D. Lukin, and P. Zoller, Phys. Rev. Lett. **106**, 220402 (2011).
[41] S.-L. Zhu, L. B. Shao, Z. D. Wang, and L. M. Duan, Phys. Rev. Lett. **106**, 100404 (2011).
[42] X.-J. Liu, L. Jiang, H. Pu, and H. Hu, Phys. Rev. A **85**, 021603(R) (2012).
[43] X. Yang and S. Wan, Phys. Rev. A **85**, 023633 (2012).
[44] K. Seo, L. Han, and C. A. R. Sá de Melo, Phys. Rev. A **85**, 033601 (2012).
[45] X.-J. Liu and H. Hu, Phys. Rev. A **85**, 033622 (2012).
[46] L. He and X.-G. Huang, Phys. Rev. A **86**, 043618 (2012).
[47] R. Wei and E. J. Mueller, Phys. Rev. A **86**, 063604 (2012).
[48] M. Iskin, Phys. Rev. A **86**, 065601 (2012).
[49] M. Gong, G. Chen, S. Jia, and C. Zhang, Phys. Rev. Lett. **109**, 105302 (2012).
[50] H. Hu, L. Jiang, H. Pu, Y. Chen, and X.-J. Liu, Phys. Rev. Lett. **110**, 020401 (2013).
[51] X.-J. Liu, Phys. Rev. A **87**, 013622 (2013).
[52] C. Chen, arXiv:1306.5934.
[53] C. Qu, Z. Zheng, M. Gong, Y. Xu, L. Mao, X. Zou, G.-C. Guo, and C. Zhang, arXiv:1307.1207.
[54] W. Zhang and W. Yi, arXiv:1307.2439.
[55] X.-J. Liu and H. Hu, Phys. Rev. A **88**, 023622 (2013).
[56] Rashba and Dresselhaus refer to two different types of SOC found in certain solids. The former occurs in crystals lacking inversion symmetry, while the latter arises in crystals lacking reflection symmetry.
[57] C. A. R. Sá de Melo, M. Randeria, and J. R. Engelbrecht, Phys. Rev. Lett. **71**, 3202 (1993).
[58] M. Randeria, in *Bose-Einstein Condensation*, edited by A. Griffin, D. W. Snoke, and S. Stringari, (Cambridge University

Press, Cambridge, England, 1995), p. 355-392.
[59] H. Hu, X.-J. Liu, and P. Drummond, Europhys. Lett. **74**, 574 (2006).
[60] R. B. Diener, R. Sensarma, and M. Randeria, Phys. Rev. A **77**, 023626 (2008).
[61] H. T. C. Stoof, K. B. Gubbels, and D. B.M. Dickerscheid, *Ultracold Quantum Fields* (Springer, 2009).
[62] H. Hu, X.-J. Liu, and P. Drummond, New J. Phys. **12**, 063038 (2010).
[63] P. Fulde and R. A. Ferrell, Phys. Rev. **135**, A550 (1964).
[64] Strictly speaking, we set the chemical potential to be the minimum energy in the two-particle continuum $2E_{\rm min}$, where $E_{\rm min}$ is the single-particle ground state energy, such that the Fermi surface shrinks and vanishes. Thus, the Fermi distribution functions in the vertex function disappear. Note that, in the vertex function the energy ω is measured with respect to the chemical potential. This procedure is exactly identical to what we have taken in the text by setting $\mu = 0$ and measuring the energy ω from zero.
[65] H. Hu, H. Pu, J. Zhang, S.-G. Peng, and X.-J. Liu, Phys. Rev. A **86**, 053627 (2012).
[66] S.-G. Peng, X.-J. Liu, H. Hu, and K. Jiang, Phys. Rev. A **86**, 063610 (2012).
[67] Q. J. Chen, J. Stajic, S. Tan, and K. Levin, Phys. Rep. **412**, 1 (2005).
[68] C. Chin, M. Bartenstein, A. Altmeyer, S. Riedl, S. Jochim, J. Hecker Denschlag, and R. Grimm, Science **305**, 1128 (2004).
[69] A. Schirotzek, Y. Shin, C. H. Schunck, and W. Ketterle, Phys. Rev. Lett. **101**, 140403 (2008).
[70] C. H. Schunck, Y. Shin, A. Schirotzek, and W. Ketterle, Nature (London) **454**, 739 (2008).
[71] J. T. Stewart, J. P. Gaebler, and D. S. Jin, Nature (London) **454**, 744 (2008).
[72] Y. Zhang, W. Ong, I. Arakelyan, J. E. Thomas, Phys. Rev. Lett. **108**, 235302 (2012).
[73] C. Kohstall, M. Zaccanti, M. Jag, A. Trenkwalder, P. Massignan, G. M. Bruun, F. Schreck and R. Grimm, Nature (London) **485**, 615 (2012).
[74] M. Koschorreck, D. Pertot, E. Vogt, B. Fröhlich, M. Feld and M. Köhl, Nature (London) **485**, 619 (2012).
[75] L. Jiang, L. O. Baksmaty, H. Hu, and H. Pu, Phys. Rev. A 83, 061604 (R) (2011).
[76] X.-J. Liu, Phys. Rev. A **86**, 033613 (2012).
[77] C. Chin and P. S. Julienne, Phys. Rev. A **71**, 012713 (2005).
[78] M. J. H. Ku, A. T. Sommer, L. W. Cheuk, and M. W. Zwierlein, Science **335**, 563 (2012).
[79] L. Radzihovsky and D. E. Sheehy, Rep. Prog. Phys. **73**, 076501 (2010).
[80] V. Barzykin and L. P. Gorkov, Phys. Rev. Lett. **89**, 227002 (2002).
[81] X.-L. Qi and S.-C. Zhang, Rev. Mod. Phys. **83**, 1057 (2011).
[82] E. Majorana, Nuovo Cimennto **14**, 171 (1937).
[83] F. Wilczek, Nature Phys. **5**, 614 (2009).
[84] C. Nayak, S. Simon, A. Stern, M. Freedman, and S. Das Sarma, Rev. Mod. Phys. **80**, 1083 (2008).
[85] G. Moore and N. Read, Nucl. Phys. **B360**, 362 (1991).
[86] N. Read and D. Green, Phys. Rev. B **61**, 10267 (2000).
[87] T. Mizushima, M. Ichioka, and K. Machida, Phys. Rev. Lett. **101**, 150409 (2008).
[88] J. D. Sau, R. M. Lutchyn, S. Tewari, and S. Das Sarma, Phys. Rev. Lett. **104**, 040502 (2010).
[89] Y. Oreg. G. Refael, and F. von Oppen, Phys. Rev. Lett. **105**, 177002 (2010).
[90] V. Mourik, K. Zuo, S. M. Frolov, S. R. Plissard, E. P. A. M. Bakkers, and L. P. Kouwenhoven, Science **336**, 1003 (2012).
[91] Another equivalent form of Rashba SOC, used extensively in the literature, is $V_{\rm SO} = \lambda(\hat{k}_x\hat{\sigma}_x + \hat{k}_y\hat{\sigma}_y)$. These are related by a spin-rotation.
[92] J. D. Sau, R. Sensarma, S. Powell, I. B. Speilman, and S. Das Sarma, Phys. Rev. B **83**, 140510(R) (2011).
[93] Z. F. Xu, and L. You, Phys. Rev. A **85**, 043605 (2012).
[94] B. M. Anderson, G. Juzeliūnas, V. M. Galitski, and I. B. Spielman, Phys. Rev. Lett. **108**, 235301 (2012).
[95] H. Zhai, Int. J. Mod. Phys. B **26**, 1230001 (2012).
[96] H. Hu and X.-J. Liu, Phys. Rev. A **85**, 013619 (2012).
[97] L. P. Gor'kov, and E. I. Rashba, Phys. Rev. Lett. **87**, 037004 (2001).
[98] S. Hoinka, M. Lingham, M. Delehaye, and C. J. Vale, Phys. Rev. Lett. **109**, 050403 (2012).
[99] K. Zhou and Z. Zhang, Phys. Rev. Lett. **108**, 025301 (2012).
[100] L. He and X.-G. Huang, Phys. Rev. Lett. **108**, 145302 (2012).
[101] D. A. Ivanov, Phys. Rev. Lett. **86**, 268 (2001).
[102] C. Caroli, P. G. de Gennes, and J. Matricon, Phys. Lett. **9**, 307 (1964).
[103] D. Wei, D. Xiong, H. Chen, and J. Zhang, Chin. Phys. Lett. **24**,679 (2007).
[104] D. Xiong, H. Chen, P. Wang, X. Yu, F. Gao and J. Zhang, Chin. Phys. Lett. **25**,843 (2008).
[105] P. Wang, H. Chen, D. Xiong, X. Yu, F. Gao and J. Zhang, Acta. Phys. Sin. **57**,4840 (2008)
[106] D. Xiong, P. Wang, Z. Fu, S. Chai, and J. Zhang, Chin. Opt. Lett. **8**,627 (2010).
[107] D. Xiong, P. Wang, Z. Fu, and J. Zhang, Opt. Exppress. **18**,1649 (2010).
[108] R. Wei and E. J. Mueller, Phys. Rev. A **87**, 042514 (2013).
[109] I. M. Lifshitz, Sov. Phys. JETP **11**, 1130 (1960).
[110] K. Jiménez-García, L. J. LeBlanc, R. A. Williams, M. C. Beeler, A. R. Perry, and I. B. Spielman, Phys. Rev. Lett. **108**, 225303 (2012).
[111] Z. F. Xu, L. You, and M. Ueda, Phys. Rev. A **87**, 063634 (2013).
[112] B. M. Anderson, I. B. Spielman, and G. Juzeliūnas, arXiv:1306.2606.